Comparison of Unsteady Aerodynamics Approximations for Time-Domain Representation of Frequency-Independent Aeroelastic State-Space Models

Ezra Tal*
Delft University of Technology, Delft, 2629 HS, Netherlands
Nhan Nguyen†
NASA Ames Research Center, Moffett Field, CA 94035
Eric Ting‡
Stinger Ghaffarian Technologies, Inc., Moffett Field, CA 94035

The advent of increasingly flexible flight vehicles calls for coupled flight dynamic and aeroelastic modeling. In general, coupled models are dependent on the reduced frequency parameter. However, this dependency is inconvenient for flight dynamic models as random gust loads, flight dynamic maneuvers, and high bandwidth control can lead to the excitation of multiple modes at varying frequencies. In this paper a method for formulating frequency-independent models using a rational fraction approximation of Theodorsen's function is presented. The method consists of regression to Theodorsen's function in the frequency domain and realization using aerodynamic lag states to obtain the frequency-independent state-space equation. While a higher order approximation will result in more accurate representation of unsteady aerodynamics, it does also result in an increased number of aerodynamic lag states. Consequently, selection of the approximation order is a trade-off between the cost of a dynamical system with an increased number of states on one hand, and the accuracy of the unsteady aerodynamics approximation on the other hand. The method is applied in order to obtain frequency-independent coupled flight dynamic and aeroelastic models of a flexible wing transport aircraft for approximations of Theodorsen's function of different orders. The resulting models are compared in both the frequency and time domain in order to assess the cost and accuracy of the approximations.

I. Introduction

In pursuit of energy efficient airframe designs the aircraft industry is utilizing modern lightweight materials, such as sophisticated composites, at increasing scale. Such materials may be able to provide sufficient load-carrying capacity at lower weight, leading to reduction of the aircraft operational empty weight (OEW). At the same time application of these materials may lead to decreased structural rigidity. With increased flexibility of the airframe, aeroelastic effects become more prominent and can significantly affect aircraft aerodynamics, potentially leading to degraded aerodynamic efficiency and decrease of control surface effectiveness.

Under the Fundamental Aeronautics Program of the NASA Aeronautics Research Mission Directorate (ARMD), the Fixed Wing/Advanced Air Transport Technology Project is conducting multidisciplinary foundational research to investigate advanced concepts and technologies for future aircraft systems. A NASA study entitled "Elastically Shaped Future Air Vehicle Concept" was conducted in 2010[1,2] to examine new

*Graduate Student, Faculty of Aerospace Engineering, e.a.tal@student.tudelft.nl, AIAA Student Member
†Research Scientist, Intelligent Systems Division, nhan.t.nguyen@nasa.gov, AIAA Associate Fellow
‡Research Engineer, Intelligent Systems Division, eric.b.ting@nasa.gov

concepts that can enable active control of wing aeroelasticity to achieve drag reduction. This study showed that highly flexible wing aerodynamic surfaces can be elastically shaped in-flight by active control of wing twist and vertical deflection in order to optimize the local angle of attack of wing sections to improve aerodynamic efficiency through drag reduction during cruise and enhanced lift performance during take-off and landing.

As aircraft structures become increasingly flexible and aeroelastic effects become more prominent, an accurate representation of flight characteristics based on a rigid-body six degrees of freedom (6DOF) flight dynamic model becomes unachievable. Structural dynamics of the aircraft are intimately coupled with flight dynamics and must be accounted for in the modeling of flexible flight vehicles. Additionally, aeroservoelastic interactions demand consideration in the control design. The mishap of the NASA Helios aircraft illustrates the complex aeroservoelasticity of flexible flight vehicles.[3] The need to assess flight performance and handling qualities and the need to design and simulate flight control systems call for coupled flight dynamic and aeroservoelastic modeling of flexible flight vehicles.

In general the coupled equations of motion are dependent on the reduced frequency parameter. This form is very useful for studying flutter since the reduced frequency is usually computed from a flutter solution. However, for flight dynamic analysis the reduced frequency dependent equation is inconvenient, since one would not know in advance which elastic modes are excited. Random gust loads, flight dynamic maneuvers, and high bandwidth control may cause the excitation of multiple modes at a range of different frequencies. A reduced frequency-dependent formulation may only be based at a single preselected frequency, leading to misrepresentation of the elastic modes acting at different frequencies. In order to address this difficulty, various approaches have been proposed.

Using the P-Transform method the most important eigenvalues and eigenvectors are calculated using a flutter solution and a state-space system is constructed based on these eigenvalues and eigenvectors. This method provides good results for low damped modes, but for modes that deviate from the flutter solution, i.e. for damped modes and forced excitations, the accuracy is reduced.[4] Frequency domain representations can also be obtained using unsteady aerodynamic computational fluid dynamics (CFD) models, for example using the Fourier transform of modal perturbation results.[5] A method for computing time domain models directly from pulse responses from CFD codes without the need to transform to the frequency domain and back has also been presented.[6] If tabulated aerodynamic force data are available for different reduced frequencies, for example from CFD analysis or experimental results, a time domain representation can be obtained using various methods, such as Padé approximants[7–9] and the well-known Roger's Rational Fractional Approximation Method.[10] On the other hand, if an analytical model of the aerodynamic forces due to elastic deformation is available, a direct approximation of Theodorsen's function[11] in the frequency domain can be used.[9,12] An approximation to Wagner's function,[13] the time domain equivalent of Theodorsen's function, which gives the circulatory lift response to a step change in upwash at the $\frac{3}{4}$ chord point,[14] is also applicable.[15,16]

In this paper a method that applies mixed real and complex linear regression to straightforwardly obtain a frequency domain approximation of any order and a corresponding state space realization is provided. The approximation method is applied in order to formulate a reduced frequency-independent elastic state space model of the Elastically Shaped Aircraft Concept (ESAC). The resulting model is then coupled to a 6DOF flight dynamic model and a comparison of the performance and cost of different order approximations is presented.

II. Overview of Elastically Shaped Aircraft Concept and Variable Camber Continuous Trailing Edge Flap

The ESAC is modeled as a notional single-aisle, mid-size, 200-passenger aircraft. The geometry of the ESAC is obtained by scaling up the geometry of the NASA Generic Transport Model (GTM) by a ratio of 200:11. The GTM is a research platform that includes a wind tunnel model and a remotely piloted vehicle, as shown in Figure 1. Figure 2 is an illustration of the GTM geometry. The reason for selecting the GTM is that there already exists an extensive wind tunnel aerodynamic database that could be used for validation in the study. The benchmark configuration represents one of the most common types of transport aircraft in the commercial aviation sector that provides short-to-medium range passenger carrying capacities.

The aircraft has a take-off weight of 200,000 lbs for a typical operating load (gear up, flap up) that includes cargo, fuel, and passengers.

Figure 1: Boeing 757 and GTM Remotely Piloted Vehicle at NASA Langley Research Center

Figure 2: GTM Geometry

To compute the mass and inertia properties of the benchmark aircraft, a component-based approach is used. The aircraft is divided into the following components: fuselage, wings, horizontal tails, vertical tail, engines, OEW equipment, and typical load including passengers, cargo, and fuel. The fuselage, wings, horizontal tails, and vertical tail are modeled as shell structures with constant wall thicknesses.[17] Based on publicly available data of component weight breakdown for various aircraft,[18] an average wing mass relative to the total empty weight of the aircraft is taken to be 24.2% of the OEW.

To enable active wing shaping control, the wing structures of the ESAC are designed to increase wing flexibility. The wing bending and torsional stiffnesses are designed to achieve a wing deflection that is about double that of a conventional aircraft wing.

For the purpose of aeroelastic shaping control a continuous flap system called the Variable Camber Continuous Trailing Edge Flap (VCCTEF) was introduced.[1,2] The VCCTEF consists of 15 flap sections attached to the outer wing and one flap section attached to the inner wing, as shown in Figure 3. Each section consists of three flap segments that can be individually commanded, as shown in Figure 4. These camber flaps are joined to the adjacent sections by a flexible and supported material with the same camber, resulting in a continuous flap system throughout the wing span with no drag producing gaps.

Using the camber positioning, a full-span, low-drag, high-lift configuration can be activated. The camber positioning is achieved using all three flap segments. The leading two segments are actuated by means of a shape memory alloy, while the trailing edge segment is actuated using a fast electro-mechanical actuator and can therefore also be applied for flight dynamic maneuvers and high-bandwidth control purposes, such as flutter suppression and gust alleviation. The bandwidth of the shape memory alloy actuator is several orders of magnitude lower than the bandwidth of the electro-mechanical actuator. Due to separation of timescales the modeling of the leading two segments is less relevant from a flight dynamic and aeroservoelastic point of view, hence the model used for the simulations presented in this paper only includes the dynamics of the 32 fast-acting trailing edge segments. The effect of the first two segments is assumed constant and can be included in the wing geometry.

Since the implementation of the unsteady aerodynamics approximation by means of lag states is similar for the VCCTEF as for the elastic wing, it was chosen to not explicitly show the equations governing the VCCTEF dynamics. The coupling of the VCCTEF model to the flight dynamic and elastic wing model is however shown.

III. Unsteady Aerodynamics Approximation

The aerodynamic forces acting on an oscillating airfoil consist of non-circulatory and circulatory contributions. The non-circulatory contribution results from the change in momentum of surrounding air due to the oscillatory motion of the airfoil. In the case of an oscillating airfoil the circulation in the bound vortex changes, and by Kelvin's circulation theorem an equal but opposite amount of circulation is added to the wake vortex. The increment in wake circulation induces a velocity increment at the airfoil, resulting in a phase lag and decrease in circulatory lift for an oscillating airfoil.

An expression for the effect of phase lag and decrease in lift as a function of the reduced frequency k of a harmonically oscillating airfoil is given by Theodorsen's function[11]

$$C(k) = F(k) + iG(k) \tag{1}$$

where $F(k) \geq 0.5$, $G(k) \leq 0$, and

$$k = \frac{\omega c}{2V} \tag{2}$$

with ω the oscillation frequency, c the airfoil chord, and V the free stream airspeed. The functions $F(k)$ and $G(k)$ are defined in terms of Bessel functions.[11]

A. Mixed Real and Complex Linear Regression

An algorithm for approximation of a complex-valued frequency response function using rational polynomials with real constants is given in this section.[19] For the present purpose of approximating Theodorsen's function the method was extended to include asymptotic constraints for $k \to 0$ and $k \to \infty$.

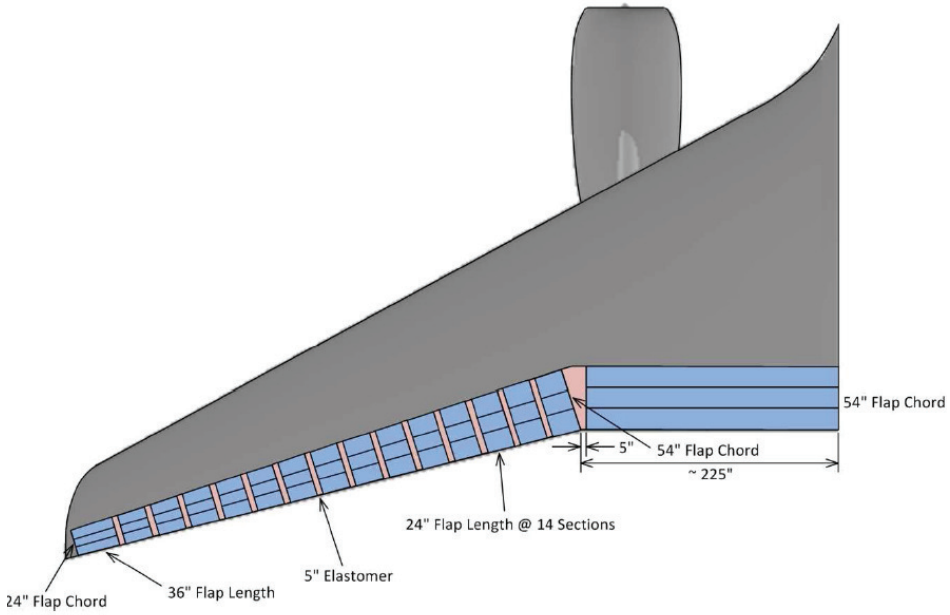

Figure 3: GTM wing with VCCTEF

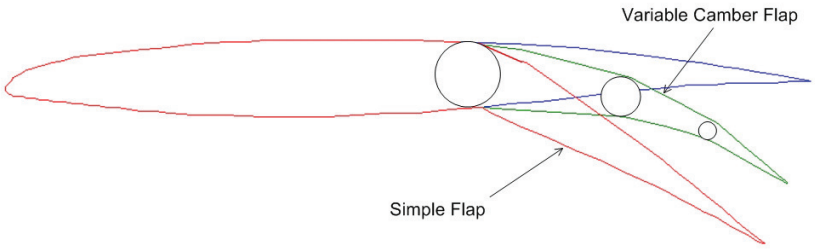

Figure 4: Variable Camber Flap

The approximation of Theodorsen's function $C(k)$ is given by the rational frequency response function

$$\bar{C}(k) = \frac{b_n(ik)^n + b_{n-1}(ik)^{n-1} + ... + b_1(ik) + b_0}{(ik)^n + a_{n-1}(ik)^{n-1} + ... + a_1(ik) + a_0} = \frac{B(k)}{A(k)} \tag{3}$$

The first asymptotic constraint $\left|\bar{C}(k)\right| \to 1$ and $\angle\bar{C}(k) \to 0$ as $k \to 0$ is satisfied by the necessary and sufficient condition that $a_0 = b_0$. It should be noted that the numerator and denominator polynomials are of the same order, i.e. the corresponding transfer function is biproper. This, together with the condition $b_n = \frac{1}{2}$, is necessary and sufficient to satisfy the second asymptotic constraint $\left|\bar{C}(k)\right| \to \frac{1}{2}$ and $\angle\bar{C}(k) \to 0$ as $k \to \infty$.

The error of the approximation is defined by

$$\varepsilon(k) = \bar{C}(k) - C(k) \tag{4}$$

The error is expressed as a function that is affine in the coefficients of $A(k)$ and $B(k)$ using the approximation

$$\bar{\varepsilon}(k) = \frac{B_m(k)}{A_{m-1}(k)} - \frac{A_m(k)}{A_{m-1}(k)}C(k) \tag{5}$$

where the subscripts indicate the regression iteration number.[19] It is apparent that as the solution converges then $\bar{\varepsilon}(k) \to \varepsilon(k)$, since $\frac{A_m(k)}{A_{m-1}(k)} \to 1$. By defining the solution vector of polynomial coefficients

$$\boldsymbol{u} = \left[\begin{array}{ccc|ccc} a_{n-1} & \cdots & a_0 & b_{n-1} & \cdots & b_1 \end{array}\right]^\top \tag{6}$$

an $w \times 1$, with w the number of frequency samples, error vector can be defined by

$$\bar{\boldsymbol{\varepsilon}} = \boldsymbol{D} + \boldsymbol{S}\boldsymbol{u} \tag{7}$$

where

$$\boldsymbol{D} = \begin{bmatrix} \left(\frac{1}{2} - C(k_1)\right)\frac{(ik_1)^n}{A_{m-1}(k_1)} \\ \vdots \\ \left(\frac{1}{2} - C(k_w)\right)\frac{(ik_w)^n}{A_{m-1}(k_w)} \end{bmatrix} \tag{8}$$

and

$$\boldsymbol{S} = \left[\begin{array}{ccc|ccc} -\frac{C(k_1)(ik_1)^{n-1}}{A_{m-1}(k_1)} & \cdots & -\frac{C(k_1)(ik_1)}{A_{m-1}(k_1)} & -\frac{C(k_1)-1}{A_{m-1}(k_1)} & \frac{(ik_1)^{n-1}}{A_{m-1}(k_1)} & \cdots & \frac{(ik_1)}{A_{m-1}(k_1)} \\ \vdots & \ddots & \vdots & \vdots & \vdots & \ddots & \vdots \\ -\frac{C(k_w)(ik_w)^{n-1}}{A_{m-1}(k_w)} & \cdots & -\frac{C(k_w)(ik_w)}{A_{m-1}(k_w)} & -\frac{C(k_w)-1}{A_{m-1}(k_w)} & \frac{(ik_w)^{n-1}}{A_{m-1}(k_w)} & \cdots & \frac{(ik_w)}{A_{m-1}(k_w)} \end{array}\right] \tag{9}$$

The cost function to be minimized is

$$\sigma^2 = (\boldsymbol{W}\boldsymbol{\varepsilon})^* (\boldsymbol{W}\boldsymbol{\varepsilon}) \tag{10}$$

where $\boldsymbol{W}$ is a weighting matrix. The asterisk denotes the conjugate transpose. The cost is minimized by iteratively solving[19]

$$\boldsymbol{u} = \mathrm{Re}\{(\boldsymbol{S}^*\boldsymbol{W}^*)(\boldsymbol{W}^*\boldsymbol{S}^*)\}^{-1}\mathrm{Re}\{(\boldsymbol{S}^*\boldsymbol{W}^*)(-\boldsymbol{W}\boldsymbol{D})\} \tag{11}$$

Existing work extends the application of Theodorsen's function to airfoils in arbitrary motion.[20,21] The imaginary variable ik can be replaced by the complex-valued reduced Laplace variable $\bar{s} = \frac{sc}{2V}$, leading to the transfer function

$$\bar{C}(\bar{s}) = \frac{b_n\bar{s}^n + b_{n-1}\bar{s}^{n-1} + ... + b_1\bar{s} + b_0}{\bar{s}^n + a_{n-1}\bar{s}^{n-1} + ... + a_1\bar{s} + a_0} \tag{12}$$

Results of the regression scheme for several values of n, along with Theodorsen's function, are shown in Figure 5. The corresponding errors are shown in Figure 6. The coefficients are given in Tables 1 and 2.

In Figure 5 it can be seen that the approximations for $n \geq 4$ are right on top of Theodorsen's function. Table 3 does indeed show that there is little added benefit to approximations of higher order.

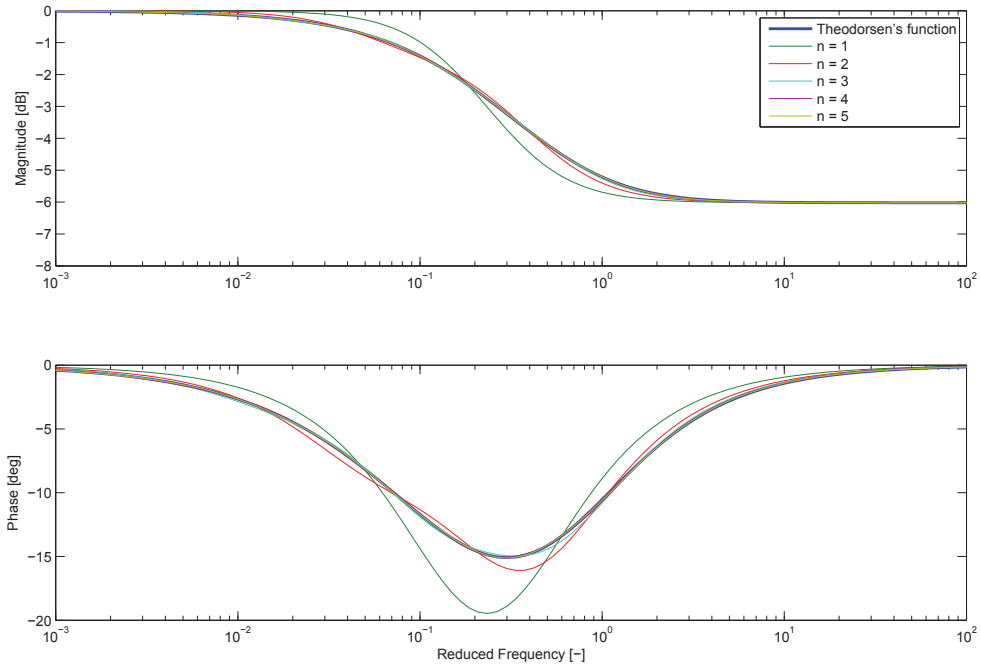

Figure 5: Frequency response plot of Theodorsen's function and approximations

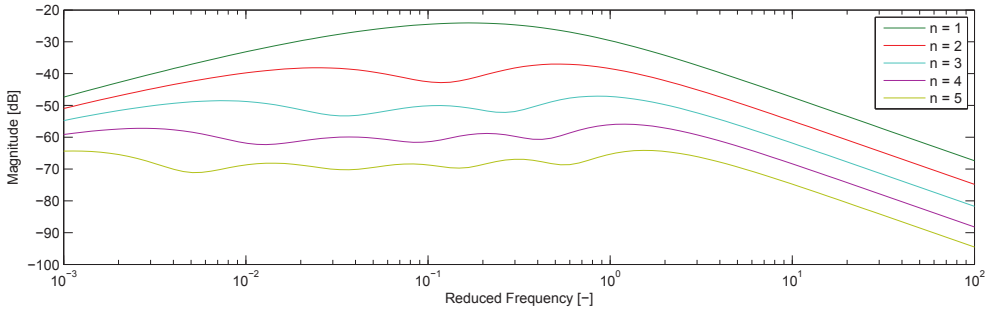

Figure 6: Magnitude of approximation errors

Table 1: Numerator coefficients of approximations

n	b_0	b_1	b_2	b_3	b_4	b_5
1	$1.646 \cdot 10^{-1}$	$5.000 \cdot 10^{-1}$				
2	$1.463 \cdot 10^{-2}$	$2.814 \cdot 10^{-1}$	$5.000 \cdot 10^{-1}$			
3	$7.891 \cdot 10^{-4}$	$5.416 \cdot 10^{-2}$	$4.020 \cdot 10^{-1}$	$5.000 \cdot 10^{-1}$		
4	$2.829 \cdot 10^{-5}$	$5.410 \cdot 10^{-3}$	$1.217 \cdot 10^{-1}$	$5.306 \cdot 10^{-1}$	$5.000 \cdot 10^{-1}$	
5	$7.960 \cdot 10^{-7}$	$3.492 \cdot 10^{-4}$	$1.936 \cdot 10^{-2}$	$2.252 \cdot 10^{-1}$	$6.724 \cdot 10^{-1}$	$5.000 \cdot 10^{-1}$

Table 2: Denominator coefficients of approximations

n	a_0	a_1	a_2	a_3	a_4
1	$1.646 \cdot 10^{-1}$				
2	$1.463 \cdot 10^{-2}$	$3.492 \cdot 10^{-1}$			
3	$7.891 \cdot 10^{-4}$	$5.876 \cdot 10^{-2}$	$5.704 \cdot 10^{-1}$		
4	$2.829 \cdot 10^{-5}$	$5.603 \cdot 10^{-3}$	$1.442 \cdot 10^{-1}$	$8.189 \cdot 10^{-1}$	
5	$7.960 \cdot 10^{-7}$	$3.552 \cdot 10^{-4}$	$2.112 \cdot 10^{-2}$	$2.891 \cdot 10^{-1}$	1.099

Table 3: Norm of error of approximations

n	$\|\varepsilon\|_\infty$ [dB]
1	-24.07
2	-36.99
3	-47.07
4	-55.89
5	-64.13

B. State-Space Realization

A minimal state-space realization of the transfer functions that are obtained using the regression scheme can be formulated in multiple forms, such as controller canonical form and forms based on partial fraction expansion. Several forms consisting of either first or second order differential equations were implemented and compared. It was found that discrepancies due to numerical differences between the state-space realizations are negligible if the realization methods are all carefully and consistently implemented while keeping numerical effects in mind. None of the realizations was found to be particularly advantageous or disadvantageous with regard to numerical stability. Differences in the sparsity of the dynamics matrices of the resulting elastic wing systems do however exist, and may lead to differences in computational cost of simulations. A realization based on full partial fraction expansion was found to give a convenient generic expression for the realization of nth-order approximations.

The approximation is first expanded into a summation of first order transfer functions. These transfer functions have real coefficients, since the poles of $\bar{C}(\bar{s})$ are all real, due to the convergent nature of Theodorsen's function. The partial fraction expansion is given by

$$\bar{C}(\bar{s}) = \frac{b_n \bar{s}^n + b_{n-1}\bar{s}^{n-1} + ... + b_1 \bar{s} + b_0}{\bar{s}^n + a_{n-1}\bar{s}^{n-1} + ... + a_1 \bar{s} + a_0} = \frac{r_n}{\bar{s} - p_n} + \frac{r_{n-1}}{\bar{s} - p_{n-1}} + ... + \frac{r_1}{\bar{s} - p_1} + k_s \tag{13}$$

where $k_s = \frac{1}{2}$ if the asymptotic contraint for $k \to \infty$ is enforced. The state-space realization of

$$\Upsilon(s) = \bar{C}(\bar{s})\Xi(s) \tag{14}$$

where $\Xi(s)$ is some input signal and $\Upsilon(s)$ is the corresponding response, is then based on the system of first order differential equations

$$v(t) = y_n + y_{n-1} + ... + y_1 + k_s \xi(t) \tag{15}$$

with

$$\frac{c}{2V}\dot{y}_n - p_n y_n = r_n \xi(t) \tag{16}$$

$$\frac{c}{2V}\dot{y}_{n-1} - p_{n-1} y_{n-1} = r_{n-1} \xi(t) \tag{17}$$

$$\vdots$$

$$\frac{c}{2V}\dot{y}_1 - p_1 y_1 = r_1 \xi(t) \tag{18}$$

and

$$\upsilon(t) = \mathscr{L}^{-1}\left\{\Upsilon(s)\right\} \tag{19}$$

$$\xi(t) = \mathscr{L}^{-1}\left\{\Xi(s)\right\} \tag{20}$$

IV. Finite Element Analysis

A vortex-lattice model of the flexible wing ESAC was developed to provide stability and control derivatives for the flight dynamic model and the aerodynamic data for the aeroelastic finite-element method (FEM).[22] The aero-propulsive-elastic equations for the ESAC were derived using the FEM based on one-dimensional structural dynamic theory that models the wing structure as a beam in a coupled bending-torsion motion.[12] For brevity only the resulting elemental system of equations is presented below.

$$\boldsymbol{M}_i \ddot{\boldsymbol{x}}_i + \boldsymbol{C}_i \dot{\boldsymbol{x}}_i + \boldsymbol{C}_i^k \boldsymbol{C}(k)\, \dot{\boldsymbol{x}}_i + \boldsymbol{K}_i \boldsymbol{x}_i + \boldsymbol{K}_i^k \boldsymbol{C}(k)\, \boldsymbol{x}_i = \boldsymbol{F}_i\left(\boldsymbol{x}_r, \dot{\boldsymbol{x}}_r, \boldsymbol{\delta}\right) \tag{21}$$

The matrices $\boldsymbol{M}_i$, $\boldsymbol{C}_i$, and $\boldsymbol{K}_i$ contain structural, propulsive, and non-circulatory aerodynamic contributions. The matrices $\boldsymbol{C}_i^k$ and $\boldsymbol{K}_i^k$ contain quasi-steady circulatory aerodynamic contributions and are multiplied with Theodorsen's function for the relevant element and degree of freedom. The vector $\boldsymbol{F}_i\left(\boldsymbol{x}_r, \dot{\boldsymbol{x}}_r, \boldsymbol{\delta}\right)$ contains external forces due to the aircraft body and VCCTEF states. The variable $\boldsymbol{\delta}$ is used to represent the complete state of the VCCTEF, including the deflections, deflection rates, deflection acceleration, and the aerodynamic lag states corresponding to VCCTEF deflection and deflection rates.

The elemental system of equations can be re-written using an nth-order approximation of Theodorsen's function. This adds $2 \times n \times d$ aerodynamic lag states per element to the model, with d the number of degrees of freedom per element, leading to the elemental equation

$$\begin{aligned}\boldsymbol{M}_i \ddot{\boldsymbol{x}}_i + \left(\boldsymbol{C}_i + k_s \boldsymbol{C}_i^k\right) \dot{\boldsymbol{x}}_i + \left(\boldsymbol{K}_i + k_s \boldsymbol{K}_i^k\right) \boldsymbol{x}_i + \boldsymbol{K}_i^k \boldsymbol{y}_{n_i} + \boldsymbol{K}_i^k \boldsymbol{y}_{n-1_i} + ... + \boldsymbol{K}_i^k \boldsymbol{y}_{1_i} \\ + \boldsymbol{C}_i^k \boldsymbol{z}_{n_i} + \boldsymbol{C}_i^k \boldsymbol{z}_{n-1_i} + ... + \boldsymbol{C}_i^k \boldsymbol{z}_{1_i} = \boldsymbol{F}_i(\boldsymbol{x}_r, \dot{\boldsymbol{x}}_r, \boldsymbol{\delta})\end{aligned} \tag{22}$$

where

$$\frac{\bar{c}_i}{2V_\infty}\dot{\boldsymbol{y}}_{n_i} + p_n \boldsymbol{y}_{n_i} = r_n \boldsymbol{x}_i \tag{23}$$

$$\frac{\bar{c}_i}{2V_\infty}\dot{\boldsymbol{y}}_{n-1_i} + p_{n-1} \boldsymbol{y}_{n-1_i} = r_{n-1} \boldsymbol{x}_i \tag{24}$$

$$\vdots$$

$$\frac{\bar{c}_i}{2V_\infty}\dot{\boldsymbol{y}}_{1_i} + p_1 \boldsymbol{y}_{1_i} = r_1 \boldsymbol{x}_i \tag{25}$$

$$\frac{\bar{c}_i}{2V_\infty}\dot{\boldsymbol{z}}_{n_i} + p_n \boldsymbol{z}_{n_i} = r_n \dot{\boldsymbol{x}}_i \tag{26}$$

$$\frac{\bar{c}_i}{2V_\infty}\dot{\boldsymbol{z}}_{n-1_i} + p_{n-1} \boldsymbol{z}_{n-1_i} = r_{n-1} \dot{\boldsymbol{x}}_i \tag{27}$$

$$\vdots$$

$$\frac{\bar{c}_i}{2V_\infty}\dot{\boldsymbol{z}}_{1_i} + p_1 \boldsymbol{z}_{1_i} = r_1 \dot{\boldsymbol{x}}_i \tag{28}$$

The discrete global approximation system is formed by enforcing equilibrium conditions at element interfaces and summing each element matrix during the assembly process, resulting in

$$\boldsymbol{M} = \sum_{i=1}^{n} \boldsymbol{M}_i \tag{29}$$

$$\boldsymbol{C} = \sum_{i=1}^{n} \left(\boldsymbol{C}_i + k_s \boldsymbol{C}_i^k \right) \tag{30}$$

$$\boldsymbol{C}^k = \sum_{i=1}^{n} \boldsymbol{C}_i^k \tag{31}$$

$$\boldsymbol{K} = \sum_{i=1}^{n} \left(\boldsymbol{K}_i + 0.5 \boldsymbol{K}_i^k \right) \tag{32}$$

$$\boldsymbol{K}^k = \sum_{i=1}^{n} \boldsymbol{K}_i^k \tag{33}$$

$$\boldsymbol{F}(\boldsymbol{x}_r, \dot{\boldsymbol{x}}_r, \boldsymbol{\delta}) = \sum_{i=1}^{n} \boldsymbol{F}_i(\boldsymbol{x}_r, \dot{\boldsymbol{x}}_r, \boldsymbol{\delta}) \tag{34}$$

$$\boldsymbol{N} = \sum_{i=1}^{n} \frac{\bar{c}_i}{2V_\infty} \tag{35}$$

where $\bar{c}_i$ is the average chord of the i-th element. The state-space equation is given by

$$
\begin{bmatrix}
\dot{\boldsymbol{x}}_e \\
\ddot{\boldsymbol{x}}_e \\
\dot{\boldsymbol{y}}_n \\
\dot{\boldsymbol{y}}_{n-1} \\
\cdots \\
\dot{\boldsymbol{y}}_1 \\
\dot{\boldsymbol{z}}_n \\
\dot{\boldsymbol{z}}_{n-1} \\
\cdots \\
\dot{\boldsymbol{z}}_1
\end{bmatrix}
=
\begin{bmatrix}
0 & \boldsymbol{I} & 0 & 0 & \cdots & 0 & 0 & 0 & \cdots & 0 \\
-\boldsymbol{M}^{-1}\boldsymbol{K} & -\boldsymbol{M}^{-1}C & -\boldsymbol{M}^{-1}\boldsymbol{K}^k & -\boldsymbol{M}^{-1}\boldsymbol{K}^k & \cdots & -\boldsymbol{M}^{-1}\boldsymbol{K}^k & -\boldsymbol{M}^{-1}\boldsymbol{C}^k & -\boldsymbol{M}^{-1}\boldsymbol{C}^k & \cdots & -\boldsymbol{M}^{-1}\boldsymbol{C}^k \\
\boldsymbol{N}^{-1}r_n & 0 & \boldsymbol{N}^{-1}p_n & 0 & \cdots & 0 & 0 & 0 & \cdots & 0 \\
\boldsymbol{N}^{-1}r_{n-1} & 0 & 0 & \boldsymbol{N}^{-1}p_{n-1} & \cdots & 0 & 0 & 0 & \cdots & 0 \\
\cdots & \cdots & \cdots & \cdots & \ddots & \cdots & \cdots & \cdots & \ddots & \cdots \\
\boldsymbol{N}^{-1}r_1 & 0 & 0 & 0 & \cdots & \boldsymbol{N}^{-1}p_1 & 0 & 0 & \cdots & 0 \\
0 & \boldsymbol{N}^{-1}r_n & 0 & 0 & \cdots & 0 & \boldsymbol{N}^{-1}p_n & 0 & \cdots & 0 \\
0 & \boldsymbol{N}^{-1}r_{n-1} & 0 & 0 & \cdots & 0 & 0 & \boldsymbol{N}^{-1}p_{n-1} & \cdots & 0 \\
\cdots & \cdots & \cdots & \cdots & \ddots & \cdots & \cdots & \cdots & \ddots & \cdots \\
0 & \boldsymbol{N}^{-1}r_1 & 0 & 0 & \cdots & 0 & 0 & 0 & \cdots & \boldsymbol{N}^{-1}p_1
\end{bmatrix}
\begin{bmatrix}
\boldsymbol{x}_e \\
\dot{\boldsymbol{x}}_e \\
\boldsymbol{y}_n \\
\boldsymbol{y}_{n-1} \\
\cdots \\
\boldsymbol{y}_1 \\
\boldsymbol{z}_n \\
\boldsymbol{z}_{n-1} \\
\cdots \\
\boldsymbol{z}_1
\end{bmatrix}
+
\begin{bmatrix}
0 \\
\boldsymbol{M}^{-1}\boldsymbol{F}(\boldsymbol{x}_r, \dot{\boldsymbol{x}}_r, \boldsymbol{\delta}) \\
0 \\
0 \\
\cdots \\
0 \\
0 \\
0 \\
\cdots \\
0
\end{bmatrix}
\tag{36}
$$

where $\boldsymbol{x}_e = \begin{bmatrix} w_1 & w_1^{'} & v_1 & v_1^{'} & \theta_1 & \dots & w_{m+1} & w_{m+1}^{'} & v_{m+1} & v_{m+1}^{'} & \theta_{m+1} \end{bmatrix}^\top$, with $m+1$ the total number of nodes, is the nodal displacement vector. Note that the aeroelastic state-space equation is coupled with aircraft flight dynamics and VCCTEF dynamics through the force term $\boldsymbol{F}(\boldsymbol{x}_r, \dot{\boldsymbol{x}}_r, \boldsymbol{\delta})$.

V. Flight Dynamic Coupling

Consider the motion of a rigid aircraft. The equations of motion that describe flight dynamics are described by the six kinematical equations

$$\dot{x} = u\cos\theta\cos\psi + v\left(-\cos\phi\sin\psi + \sin\phi\sin\theta\cos\psi\right) + w\left(\sin\phi\sin\psi + \cos\phi\sin\theta\cos\psi\right) \tag{37}$$

$$\dot{y} = u\cos\theta\sin\psi + v\left(\cos\phi\cos\psi + \sin\phi\sin\theta\sin\psi\right) + w\left(-\sin\phi\cos\psi + \cos\phi\sin\theta\sin\psi\right) \tag{38}$$

$$\dot{h} = u\sin\theta - v\sin\phi\cos\theta - w\cos\phi\cos\theta \tag{39}$$

$$\dot{\phi} = p + q\sin\phi\tan\theta + r\cos\phi\tan\theta \tag{40}$$

$$\dot{\theta} = q\cos\phi - r\sin\phi \tag{41}$$

$$\dot{\psi} = q\sin\phi\sec\theta + r\cos\phi\sec\theta \tag{42}$$

and six dynamical equations

$$m_a\left(\dot{u} + qw - rv\right) = C_X q_\infty S + T - m_a g\sin\theta \tag{43}$$

$$m_a\left(\dot{v} + ru - pw\right) = C_Y q_\infty S + m_a g\cos\theta\sin\phi \tag{44}$$

$$m_a\left(\dot{w} + pv - qu\right) = C_Z q_\infty S + m_a g\cos\theta\cos\phi \tag{45}$$

$$\bar{I}_{xx}\dot{p} - \bar{I}_{xy}\dot{q} - \bar{I}_{xz}\dot{r} - \bar{I}_{xz}pq + \bar{I}_{xy}pr + \left(\bar{I}_{zz} - \bar{I}_{yy}\right)qr + \bar{I}_{yz}\left(r^2 - q^2\right) = C_l q_\infty S b \tag{46}$$

$$-\bar{I}_{xy}\dot{p} + \bar{I}_{yy}\dot{q} - \bar{I}_{yz}\dot{r} + \bar{I}_{yz}pq - \bar{I}_{xy}qr + \left(\bar{I}_{xx} - \bar{I}_{zz}\right)pr + \bar{I}_{xz}\left(p^2 - r^2\right) = C_m q_\infty S\bar{c} + T z_e \tag{47}$$

$$-\bar{I}_{xz}\dot{p} - \bar{I}_{yz}\dot{q} + \bar{I}_{zz}\dot{r} - \bar{I}_{yz}pr + \bar{I}_{xz}qr + \left(\bar{I}_{yy} - \bar{I}_{xx}\right)pq + \bar{I}_{xy}\left(q^2 - p^2\right) = C_n q_\infty S b \tag{48}$$

where m_a is the aircraft mass; S is the aircraft reference wing area; $\bar{I}_{xx}$, $\bar{I}_{yy}$, $\bar{I}_{zz}$, $\bar{I}_{xy}$, $\bar{I}_{xz}$, $\bar{I}_{yz}$ are the aircraft principal moment of inertia; $\bar{c}$ is the mean aerodynamic chord; b is the wing span; z_e is the offset of the thrust line below the aircraft CG; ϕ, θ, ψ are the aircraft Euler angles, and C_X, C_Y, and C_Z are the force coefficients expressed in the aircraft body fixed reference frame.

A. Unsteady Aerodynamic Coefficients due to Aeroelasticity

The aerodynamic coefficients C_L, C_D, C_y, C_l, C_m, and C_n are influenced by the aeroelastic deflections of the aircraft wings. Therefore, the flight dynamic equations of motion of the aircraft are coupled with the aeroelastic equations via the aerodynamic coefficients. The motion can be decomposed into symmetric and anti-symmetric motions. The lift, drag, and pitching moment coefficients are influenced by symmetric aeroelastic modes, while the side force, rolling moment, and yawing moment coefficients are influenced by anti-symmetric aeroelastic modes.

Due to the joining of the VVCTEF segments to the elastic wing, the wing deformation will also cause an aerodynamic hinge moment on the flap hinges. The corresponding coefficients are indicated as $C_{H_{i_f}}$ with $i_f \in \{1, 2, .., 32\}$ the index of the appropriate fast-acting flap segment.

The aeroelastic contributions to the aerodynamic coefficients are expressed as

$$\Delta C_a = \boldsymbol{C}_{a_{\ddot{\boldsymbol{x}}_e}}\ddot{\boldsymbol{x}}_e + \boldsymbol{C}_{a_{\dot{\boldsymbol{x}}_e}}\dot{\boldsymbol{x}}_e + \boldsymbol{C}_{a_{\boldsymbol{x}_e}}\boldsymbol{x}_e + \begin{bmatrix} \boldsymbol{C}_{a_{\boldsymbol{y}_a}} & \boldsymbol{C}_{a_{\boldsymbol{y}_a}} & \cdots & \boldsymbol{C}_{a_{\boldsymbol{y}_a}} \end{bmatrix}\boldsymbol{y}_a + \begin{bmatrix} \boldsymbol{C}_{a_{\boldsymbol{z}_a}} & \boldsymbol{C}_{a_{\boldsymbol{z}_a}} & \cdots & \boldsymbol{C}_{a_{\boldsymbol{z}_a}} \end{bmatrix}\boldsymbol{z}_a \tag{49}$$

where C_a is a dummy notation that stands for C_L, C_D, C_Y, C_l, C_m, C_n or C_{H_i},
$\boldsymbol{y}_a = \begin{bmatrix} \boldsymbol{y}_n{}^\top & \boldsymbol{y}_{n-1}{}^\top & \cdots & \boldsymbol{y}_1{}^\top \end{bmatrix}^\top$ and $\boldsymbol{z}_a = \begin{bmatrix} \boldsymbol{z}_n{}^\top & \boldsymbol{z}_{n-1}{}^\top & \cdots & \boldsymbol{z}_1{}^\top \end{bmatrix}^\top$ are aerodynamic lag states, and

$$\boldsymbol{C}_{a_{\ddot{\boldsymbol{x}}_e}} = \sum_{i=1}^{n} \boldsymbol{C}_{a_{\ddot{\boldsymbol{x}}_i}} \tag{50}$$

$$\boldsymbol{C}_{a_{\dot{\boldsymbol{x}}_e}} = \sum_{i=1}^{n} \left(\boldsymbol{C}_{a_{\dot{\boldsymbol{x}}_i}} + k_s \boldsymbol{C}^k_{a_{\dot{\boldsymbol{x}}_i}} \right) \tag{51}$$

$$\boldsymbol{C}_{a_{\boldsymbol{x}_e}} = \sum_{i=1}^{n} \left(k_s \boldsymbol{C}^k_{a_{\boldsymbol{x}_i}} \right) \tag{52}$$

$$\boldsymbol{C}_{a_{\boldsymbol{y}_a}} = \sum_{i=1}^{n} \boldsymbol{C}^k_{a_{\boldsymbol{x}_i}} \tag{53}$$

$$\boldsymbol{C}_{a_{\boldsymbol{z}_a}} = \sum_{i=1}^{n} \boldsymbol{C}^k_{a_{\dot{\boldsymbol{x}}_i}} \tag{54}$$

with again the superscript k indicating the circulatory aerodynamic contributions. The aircraft flight dynamic equation is then expressed as

$$\dot{\boldsymbol{x}}_r = f\left(\dot{\boldsymbol{x}}_r, \boldsymbol{x}_r, \ddot{\boldsymbol{x}}_e, \dot{\boldsymbol{x}}_e, \boldsymbol{x}_e, \boldsymbol{y}_a, \boldsymbol{z}_a, \boldsymbol{\delta}, \delta_e, \delta_r\right) \tag{55}$$

which is coupled with the flexible wing aeroelastic state-space equation.

B. Modal Decoupling

The aeroelastic state-space equation can be expressed in terms of the generalized coordinates $\boldsymbol{\eta}$ by the coordinate transformation $\boldsymbol{x}_e = \boldsymbol{\Phi}\boldsymbol{\eta}$, where $\boldsymbol{\Phi}$ is the eigenfunction matrix. By pre-multiplying the transformed aeroelastic state-space equation by $\boldsymbol{\Phi}^\top$, this results in

$$\boldsymbol{\Phi}^\top \boldsymbol{M}\boldsymbol{\Phi}\ddot{\boldsymbol{\eta}} + \boldsymbol{\Phi}^\top \boldsymbol{C}\boldsymbol{\Phi}\dot{\boldsymbol{\eta}} + \boldsymbol{\Phi}^\top \boldsymbol{K}\boldsymbol{\Phi}\boldsymbol{\eta} + \boldsymbol{\Phi}^\top \boldsymbol{L}\boldsymbol{y}_a + \boldsymbol{\Phi}^\top \boldsymbol{O}\boldsymbol{z}_a = \boldsymbol{\Phi}^\top \boldsymbol{F}\left(\dot{\boldsymbol{x}}_r, \boldsymbol{x}_r, \boldsymbol{\delta}\right) \tag{56}$$

where $\boldsymbol{L} = \begin{bmatrix} \boldsymbol{K}^k & \boldsymbol{K}^k & \cdots & \boldsymbol{K}^k \end{bmatrix}$ and $\boldsymbol{O} = \begin{bmatrix} \boldsymbol{C}^k & \boldsymbol{C}^k & \cdots & \boldsymbol{C}^k \end{bmatrix}$. The generalized aeroelastic state-space equation can be partitioned as

$$\begin{bmatrix} \boldsymbol{M}_{oo} & \boldsymbol{M}_{oe} \\ \boldsymbol{M}_{eo} & \boldsymbol{M}_{ee} \end{bmatrix} \begin{bmatrix} \ddot{\boldsymbol{\eta}}_o \\ \ddot{\boldsymbol{\eta}}_e \end{bmatrix} + \begin{bmatrix} \boldsymbol{C}_{oo} & \boldsymbol{C}_{oe} \\ \boldsymbol{C}_{eo} & \boldsymbol{C}_{ee} \end{bmatrix} \begin{bmatrix} \dot{\boldsymbol{\eta}}_o \\ \dot{\boldsymbol{\eta}}_e \end{bmatrix} + \begin{bmatrix} \boldsymbol{K}_{oo} & \boldsymbol{K}_{oe} \\ \boldsymbol{K}_{eo} & \boldsymbol{K}_{ee} \end{bmatrix} \begin{bmatrix} \boldsymbol{\eta}_o \\ \boldsymbol{\eta}_e \end{bmatrix} + \begin{bmatrix} \boldsymbol{L}_o \\ \boldsymbol{L}_e \end{bmatrix} \boldsymbol{y}_a + \begin{bmatrix} \boldsymbol{O}_o \\ \boldsymbol{O}_e \end{bmatrix} \boldsymbol{z}_a = \begin{bmatrix} \boldsymbol{F}_{o_{\dot{\boldsymbol{x}}_r}} \\ \boldsymbol{F}_{e_{\dot{\boldsymbol{x}}_r}} \end{bmatrix} \dot{\boldsymbol{x}}_r + \begin{bmatrix} \boldsymbol{F}_{o_{\boldsymbol{x}_r}} \\ \boldsymbol{F}_{e_{\boldsymbol{x}_r}} \end{bmatrix} \boldsymbol{x}_r + \begin{bmatrix} \boldsymbol{F}_{o_{\boldsymbol{\delta}}} \\ \boldsymbol{F}_{e_{\boldsymbol{\delta}}} \end{bmatrix} \boldsymbol{\delta} \tag{57}$$

where $\boldsymbol{\eta}_o$ is the generalized coordinate vector of the rigid-body modes which needs to be eliminated as it is already accounted for in the 6DOF nonlinear flight dynamic model, and $\boldsymbol{F}_{o_{\dot{\boldsymbol{x}}_r}}$, $\boldsymbol{F}_{e_{\dot{\boldsymbol{x}}_r}}$, $\boldsymbol{F}_{o_{\boldsymbol{x}_r}}$, $\boldsymbol{F}_{e_{\boldsymbol{x}_r}}$, $\boldsymbol{F}_{o_{\boldsymbol{\delta}}}$, and $\boldsymbol{F}_{e_{\boldsymbol{\delta}}}$ are the generalized aerodynamic forces due to the flight dynamic and control states.[12]

Note that, while the nodal displacement vector is transformed into the generalized coordinate reference frame, the aerodynamic lag state vectors $\boldsymbol{y}_a$ and $\boldsymbol{z}_a$ remain in the physical coordinate reference frame. The aerodynamic lag states can straightforwardly be transformed to the generalized coordinate reference frame in the same manner as the nodal displacement vector is transformed. This may especially be beneficial for the creation of a reduced order model.

The incremental aerodynamic coefficients due to wing aeroelasticity are transformed into the generalized coordinates

$$\boldsymbol{C}_{a_{\ddot{\boldsymbol{\eta}}_e}} = \boldsymbol{C}_{a_{\ddot{\boldsymbol{x}}_o}} \boldsymbol{\Phi}_{oe} + \boldsymbol{C}_{a_{\ddot{\boldsymbol{x}}_e}} \boldsymbol{\Phi}_{ee} \tag{58}$$

$$\boldsymbol{C}_{a_{\dot{\boldsymbol{\eta}}_e}} = \boldsymbol{C}_{a_{\dot{\boldsymbol{x}}_o}} \boldsymbol{\Phi}_{oe} + \boldsymbol{C}_{a_{\dot{\boldsymbol{x}}_e}} \boldsymbol{\Phi}_{ee} \tag{59}$$

$$\boldsymbol{C}_{a_{\boldsymbol{\eta}_e}} = \boldsymbol{C}_{a_{\boldsymbol{x}_o}} \boldsymbol{\Phi}_{oe} + \boldsymbol{C}_{a_{\boldsymbol{x}_e}} \boldsymbol{\Phi}_{ee} \tag{60}$$

where $\boldsymbol{\Phi}_{oe}$, and $\boldsymbol{\Phi}_{ee}$ are partitioned matrices of $\boldsymbol{\Phi}$.

C. Coupled State-Space Equation

For the purpose of coupling the aeroelastic equation with a nonlinear 6DOF flight dynamic model an aeroelastic state-space system with inputs $\dot{\boldsymbol{x}}_r$, $\boldsymbol{x}_r$, and $\boldsymbol{\delta}$ is formulated. The system's outputs ΔC_a are fed back into the flight dynamic model. In case the aeroelastic equation is to be coupled with a linear flight dynamic model, for example in order to perform eigenvalue analysis of the coupled system, this can be done straightforwardly by expanding the matrices $\bar{\boldsymbol{M}}$ and $\bar{\boldsymbol{S}}$ with elements from $\bar{\boldsymbol{D}}$, $\bar{\boldsymbol{E}}$, $\bar{\boldsymbol{G}}$, and the flight dynamic state-space equation

$$\bar{\boldsymbol{M}} \begin{bmatrix} \dot{\boldsymbol{x}}_s \\ \dot{\boldsymbol{x}}_a \end{bmatrix} = \bar{\boldsymbol{S}} \begin{bmatrix} \boldsymbol{x}_s \\ \boldsymbol{x}_a \end{bmatrix} + \bar{\boldsymbol{E}} \begin{bmatrix} \dot{\boldsymbol{x}}_r \\ \boldsymbol{x}_r \\ \boldsymbol{\delta} \end{bmatrix} \tag{61}$$

$$[\boldsymbol{C}_e] = \bar{\boldsymbol{D}} \begin{bmatrix} \dot{\boldsymbol{x}}_s \\ \dot{\boldsymbol{x}}_a \end{bmatrix} + \bar{\boldsymbol{G}} \begin{bmatrix} \boldsymbol{x}_s \\ \boldsymbol{x}_a \end{bmatrix} \tag{62}$$

where $\boldsymbol{x}_s = \begin{bmatrix} \boldsymbol{\eta}_e & \dot{\boldsymbol{\eta}}_e \end{bmatrix}^\top$ is the elastic state vector, $\boldsymbol{x}_a = \begin{bmatrix} \boldsymbol{y}_a & \boldsymbol{z}_a \end{bmatrix}^\top$ is the aerodynamic lag state vector, and $\boldsymbol{C}_e = \begin{bmatrix} \Delta C_L & \Delta C_D & \Delta C_Y & \Delta C_l & \Delta C_m & \Delta C_n & \Delta \boldsymbol{C}_H{}^\top \end{bmatrix}^\top$, with $\Delta \boldsymbol{C}_H = \begin{bmatrix} \Delta C_{H_1} & \Delta C_{H_2} & \cdots & \Delta C_{H_{32}} \end{bmatrix}^\top$, contains the incremental aerodynamic coefficients due to wing aeroelasticity. The matrices are defined as

$$\bar{\boldsymbol{M}} = \begin{bmatrix} \boldsymbol{M}_{ss} & 0 \\ 0 & \boldsymbol{M}_{aa} \end{bmatrix} \tag{63}$$

$$\bar{\boldsymbol{S}} = \begin{bmatrix} \boldsymbol{S}_{ss} & \boldsymbol{S}_{sa} \\ \boldsymbol{S}_{as} & \boldsymbol{S}_{aa} \end{bmatrix} \tag{64}$$

$$\bar{\boldsymbol{E}} = \begin{bmatrix} \boldsymbol{E}_{\dot{\boldsymbol{x}}_r} & \boldsymbol{E}_{\boldsymbol{x}_r} & \boldsymbol{E}_{\boldsymbol{\delta}} \\ 0 & 0 & 0 \end{bmatrix} \tag{65}$$

$$\bar{\boldsymbol{D}} = \begin{bmatrix} \boldsymbol{D}_s & 0 \end{bmatrix} \tag{66}$$

$$\bar{\boldsymbol{G}} = \begin{bmatrix} \boldsymbol{G}_s & \boldsymbol{G}_a \end{bmatrix} \tag{67}$$

where

$$\boldsymbol{M}_{ss} = \begin{bmatrix} \boldsymbol{I} & 0 \\ 0 & \boldsymbol{M}_{ee} \end{bmatrix} \tag{68}$$

$$\boldsymbol{M}_{aa} = \boldsymbol{I} \otimes \boldsymbol{N} \tag{69}$$

$$\boldsymbol{S}_{ss} = \begin{bmatrix} 0 & \boldsymbol{I} \\ -\boldsymbol{K}_{ee} & -\boldsymbol{C}_{ee} \end{bmatrix} \tag{70}$$

$$\boldsymbol{S}_{sa} = \begin{bmatrix} 0 & 0 \\ -\boldsymbol{L}_e & -\boldsymbol{O}_e \end{bmatrix} \tag{71}$$

$$\tag{72}$$

$$\boldsymbol{S}_{as} = \begin{bmatrix} \begin{bmatrix} r_n \\ r_{n-1} \\ \vdots \\ r_1 \end{bmatrix} \otimes \begin{bmatrix} \boldsymbol{\Phi}_{oe} \\ \boldsymbol{\Phi}_{ee} \end{bmatrix} & 0 \\ 0 & \begin{bmatrix} r_n \\ r_{n-1} \\ \vdots \\ r_1 \end{bmatrix} \otimes \begin{bmatrix} \boldsymbol{\Phi}_{oe} \\ \boldsymbol{\Phi}_{ee} \end{bmatrix} \end{bmatrix} \tag{73}$$

$$\boldsymbol{S}_{aa} = \begin{bmatrix} p_n & 0 & \cdots & 0 \\ 0 & p_{n-1} & \cdots & 0 \\ \vdots & \vdots & \ddots & \vdots \\ 0 & 0 & \cdots & p_1 \end{bmatrix} \otimes \boldsymbol{I} \tag{74}$$

$$\boldsymbol{E}_{\dot{\boldsymbol{x}}_r} = \begin{bmatrix} 0 \\ \boldsymbol{F}_{e_{\dot{\boldsymbol{x}}_r}} \end{bmatrix} \tag{75}$$

$$\boldsymbol{E}_{\boldsymbol{x}_r} = \begin{bmatrix} 0 \\ \boldsymbol{F}_{e_{\boldsymbol{x}_r}} \end{bmatrix} \tag{76}$$

$$\boldsymbol{E}_{\boldsymbol{\delta}} = \begin{bmatrix} 0 \\ \boldsymbol{F}_{e_{\boldsymbol{\delta}}} \end{bmatrix} \tag{77}$$

$$\boldsymbol{D}_s = \begin{bmatrix} 0 & 0 & 0 & 0 & 0 & 0 & 0 \\ \boldsymbol{C}_{L_{\ddot{\boldsymbol{\eta}}_e}} & \boldsymbol{C}_{D_{\ddot{\boldsymbol{\eta}}_e}} & \boldsymbol{C}_{Y_{\ddot{\boldsymbol{\eta}}_e}} & \boldsymbol{C}_{l_{\ddot{\boldsymbol{\eta}}_e}} & \boldsymbol{C}_{m_{\ddot{\boldsymbol{\eta}}_e}} & \boldsymbol{C}_{n_{\ddot{\boldsymbol{\eta}}_e}} & \boldsymbol{C}_{H_{\ddot{\boldsymbol{\eta}}_e}}{}^{\top} \end{bmatrix}^{\top} \tag{78}$$

$$\boldsymbol{G}_s = \begin{bmatrix} \boldsymbol{C}_{L_{\boldsymbol{\eta}_e}} & \boldsymbol{C}_{D_{\boldsymbol{\eta}_e}} & \boldsymbol{C}_{Y_{\boldsymbol{\eta}_e}} & \boldsymbol{C}_{l_{\boldsymbol{\eta}_e}} & \boldsymbol{C}_{m_{\boldsymbol{\eta}_e}} & \boldsymbol{C}_{n_{\boldsymbol{\eta}_e}} & \boldsymbol{C}_{H_{\boldsymbol{\eta}_e}}{}^{\top} \\ \boldsymbol{C}_{L_{\dot{\boldsymbol{\eta}}_e}} & \boldsymbol{C}_{D_{\dot{\boldsymbol{\eta}}_e}} & \boldsymbol{C}_{Y_{\dot{\boldsymbol{\eta}}_e}} & \boldsymbol{C}_{l_{\dot{\boldsymbol{\eta}}_e}} & \boldsymbol{C}_{m_{\dot{\boldsymbol{\eta}}_e}} & \boldsymbol{C}_{n_{\dot{\boldsymbol{\eta}}_e}} & \boldsymbol{C}_{H_{\dot{\boldsymbol{\eta}}_e}}{}^{\top} \end{bmatrix}^{\top} \tag{79}$$

$$\boldsymbol{G}_a = \begin{bmatrix} \boldsymbol{C}_{L_{\boldsymbol{y}_a}} & \boldsymbol{C}_{L_{\boldsymbol{y}_a}} & \cdots & \boldsymbol{C}_{L_{\boldsymbol{y}_a}} & \boldsymbol{C}_{L_{\boldsymbol{z}_a}} & \boldsymbol{C}_{L_{\boldsymbol{z}_a}} & \cdots & \boldsymbol{C}_{L_{\boldsymbol{z}_a}} \\ \boldsymbol{C}_{D_{\boldsymbol{y}_a}} & \boldsymbol{C}_{D_{\boldsymbol{y}_a}} & \cdots & \boldsymbol{C}_{D_{\boldsymbol{y}_a}} & \boldsymbol{C}_{D_{\boldsymbol{z}_a}} & \boldsymbol{C}_{D_{\boldsymbol{z}_a}} & \cdots & \boldsymbol{C}_{D_{\boldsymbol{z}_a}} \\ \boldsymbol{C}_{Y_{\boldsymbol{y}_a}} & \boldsymbol{C}_{Y_{\boldsymbol{y}_a}} & \cdots & \boldsymbol{C}_{Y_{\boldsymbol{y}_a}} & \boldsymbol{C}_{Y_{\boldsymbol{z}_a}} & \boldsymbol{C}_{Y_{\boldsymbol{z}_a}} & \cdots & \boldsymbol{C}_{Y_{\boldsymbol{z}_a}} \\ \boldsymbol{C}_{l_{\boldsymbol{y}_a}} & \boldsymbol{C}_{l_{\boldsymbol{y}_a}} & \cdots & \boldsymbol{C}_{l_{\boldsymbol{y}_a}} & \boldsymbol{C}_{l_{\boldsymbol{z}_a}} & \boldsymbol{C}_{l_{\boldsymbol{z}_a}} & \cdots & \boldsymbol{C}_{l_{\boldsymbol{z}_a}} \\ \boldsymbol{C}_{m_{\boldsymbol{y}_a}} & \boldsymbol{C}_{m_{\boldsymbol{y}_a}} & \cdots & \boldsymbol{C}_{m_{\boldsymbol{y}_a}} & \boldsymbol{C}_{m_{\boldsymbol{z}_a}} & \boldsymbol{C}_{m_{\boldsymbol{z}_a}} & \cdots & \boldsymbol{C}_{m_{\boldsymbol{z}_a}} \\ \boldsymbol{C}_{n_{\boldsymbol{y}_a}} & \boldsymbol{C}_{n_{\boldsymbol{y}_a}} & \cdots & \boldsymbol{C}_{n_{\boldsymbol{y}_a}} & \boldsymbol{C}_{n_{\boldsymbol{z}_a}} & \boldsymbol{C}_{n_{\boldsymbol{z}_a}} & \cdots & \boldsymbol{C}_{n_{\boldsymbol{z}_a}} \\ \boldsymbol{C}_{H_{\boldsymbol{y}_a}} & \boldsymbol{C}_{H_{\boldsymbol{y}_a}} & \cdots & \boldsymbol{C}_{H_{\boldsymbol{y}_a}} & \boldsymbol{C}_{H_{\boldsymbol{z}_a}} & \boldsymbol{C}_{H_{\boldsymbol{z}_a}} & \cdots & \boldsymbol{C}_{H_{\boldsymbol{z}_a}} \end{bmatrix} \tag{80}$$

VI. Modal Analysis

An eigenvalue analysis of the coupled system is performed in order to assess the influence of the unsteady aerodynamics approximation on the frequency and damping of the flight dynamic and aeroelastic modes. The linearized coupled system is obtained by trimming the coupled nonlinear flight dynamic and linear aeroelastic system using the elevator, and then linearizing the flight dynamic equation at the trim condition. The trimming routine gives the same results for all approximations, since it calculates a static aeroelastic solution that is a function of the steady-state gain of the approximating transfer function. This steady-state gain is equal for all approximations because of the asymptotic constraint at $k \to 0$.

A. Coupled Flight Dynamic and Elastic Modes

Due to the coupling of flight dynamic and aeroelasic modes, the unsteady aerodynamics approximation does not only influence frequency and damping of the aeroelastic modes, but also of the flight dynamic modes. An overview of the pole locations for oscillatory flight dynamic modes and the first six aeroelastic modes in cruise flight at Mach 0.797 and 36,000 ft altitude for various approximations is given in Tables 4, 5, and

6. Values are also given for a frequency-dependent model. The term frequency-dependent herein refers to a coupled flight dynamic and aeroelastic model without lag states, i.e. with a constant complex value for $C(k)$ that is set using a preselected frequency.[12] The preselected frequency is set at the frequency of the first elastic wing mode, i.e. the mode that is closest in frequency to the aircraft body modes.

The shapes of the first six structural elastic modes are shown in Figure 7. The structural mode shapes are determined using the structural mass and stiffness matrices and are thus independent of the unsteady aerodynamics approximation. The pole locations in Tables 5 and 6 correspond to the aeroelastic modes in cruise flight. Due to aerodynamic coupling of modes the aeroelastic modes are slightly differently shaped.

Table 4: Pole locations of oscillatory flight dynamic modes of ESAC at Mach 0.797 and 36,000 ft altitude for rigid-body (RB), frequency-dependent (FD) at $\omega = 9$ rad/s, and approximation models

n	Phugoid	Short Period	Dutch Roll
RB	$-7.0837 \cdot 10^{-4} \pm 6.7051 \cdot 10^{-2} i$	$-6.9114 \cdot 10^{-1} \pm 1.4277 i$	$-3.1879 \cdot 10^{-1} \pm 1.4308 i$
FD	$-1.2386 \cdot 10^{-4} \pm 6.7977 \cdot 10^{-2} i$	$-6.5416 \cdot 10^{-1} \pm 1.3862 i$	$-3.4926 \cdot 10^{-1} \pm 1.4541 i$
1	$-1.1410 \cdot 10^{-4} \pm 6.8021 \cdot 10^{-2} i$	$-6.4592 \cdot 10^{-1} \pm 1.3817 i$	$-3.4911 \cdot 10^{-1} \pm 1.4527 i$
2	$-1.1465 \cdot 10^{-4} \pm 6.8021 \cdot 10^{-2} i$	$-6.4494 \cdot 10^{-1} \pm 1.3802 i$	$-3.4933 \cdot 10^{-1} \pm 1.4527 i$
3	$-1.1508 \cdot 10^{-4} \pm 6.8021 \cdot 10^{-2} i$	$-6.4614 \cdot 10^{-1} \pm 1.3785 i$	$-3.4943 \cdot 10^{-1} \pm 1.4528 i$
4	$-1.1540 \cdot 10^{-4} \pm 6.8021 \cdot 10^{-2} i$	$-6.4722 \cdot 10^{-1} \pm 1.3800 i$	$-3.4936 \cdot 10^{-1} \pm 1.4528 i$
5	$-1.1548 \cdot 10^{-4} \pm 6.8021 \cdot 10^{-2} i$	$-6.4627 \cdot 10^{-1} \pm 1.3799 i$	$-3.4938 \cdot 10^{-1} \pm 1.4528 i$

Table 5: Pole locations of symmetric aeroelastic modes of ESAC at Mach 0.797 and 36,000 ft altitude for frequency-dependent (FD) at $\omega = 9$ rad/s, and approximation models

n	First Mode	Second Mode	Third Mode
FD	$-6.9276 \cdot 10^{-1} \pm 9.0032 i$	$-3.3504 \cdot 10^{-1} \pm 21.410 i$	$-1.0155 \pm 23.291 i$
1	$-8.1369 \cdot 10^{-1} \pm 9.2633 i$	$-3.8582 \cdot 10^{-1} \pm 21.439 i$	$-8.4195 \cdot 10^{-1} \pm 23.300 i$
2	$-6.8942 \cdot 10^{-1} \pm 9.0952 i$	$-4.9909 \cdot 10^{-1} \pm 21.253 i$	$-6.9739 \cdot 10^{-1} \pm 23.256 i$
3	$-7.4991 \cdot 10^{-1} \pm 9.0970 i$	$-4.6759 \cdot 10^{-1} \pm 21.285 i$	$-7.1627 \cdot 10^{-1} \pm 23.271 i$
4	$-7.3394 \cdot 10^{-1} \pm 9.0933 i$	$-4.8307 \cdot 10^{-1} \pm 21.284 i$	$-7.1428 \cdot 10^{-1} \pm 23.261 i$
5	$-7.3981 \cdot 10^{-1} \pm 9.0957 i$	$-4.7962 \cdot 10^{-1} \pm 21.280 i$	$-7.1216 \cdot 10^{-1} \pm 23.264 i$

Table 6: Pole locations of asymmetric aeroelastic modes of ESAC at Mach 0.797 and 36,000 ft altitude for frequency-dependent (FD) at $\omega = 9$ rad/s, and approximation models

n	First Mode	Second Mode	Third Mode
FD	$-7.1968 \cdot 10^{-1} \pm 14.613 i$	$-8.4312 \cdot 10^{-1} \pm 22.742 i$	$-1.4565 \pm 33.834 i$
1	$-8.0301 \cdot 10^{-1} \pm 14.703 i$	$-7.0508 \cdot 10^{-1} \pm 22.835 i$	$-9.0543 \cdot 10^{-1} \pm 33.820 i$
2	$-7.9338 \cdot 10^{-1} \pm 14.428 i$	$-6.0730 \cdot 10^{-1} \pm 22.808 i$	$-9.3867 \cdot 10^{-1} \pm 33.700 i$
3	$-8.1273 \cdot 10^{-1} \pm 14.479 i$	$-6.1898 \cdot 10^{-1} \pm 22.820 i$	$-9.0840 \cdot 10^{-1} \pm 33.706 i$
4	$-8.1596 \cdot 10^{-1} \pm 14.462 i$	$-6.1837 \cdot 10^{-1} \pm 22.813 i$	$-9.1535 \cdot 10^{-1} \pm 33.714 i$
5	$-8.1303 \cdot 10^{-1} \pm 14.466 i$	$-6.1665 \cdot 10^{-1} \pm 22.815 i$	$-9.1707 \cdot 10^{-1} \pm 33.710 i$

It can be seen that the coupling of the flight dynamic model to the aeroelastic wing model has a large influence on frequency and damping of the oscillatory flight dynamic modes. Inspection of Table 4 shows that even for low values of n the frequency-independent models are able to approximate the coupled flight dynamic modes quite well. The pole locations of the frequency-dependent model clearly deviate somewhat, but are still close to those of the approximation models. This is also shown in Figure 8, where the poles corresponding to the flight dynamic modes from all of the coupled models are right on top of each other.

The frequency-dependent model is most accurate for modes around the preselected frequency $\omega = 9$ rad/s. These are the modes that are most strongly coupled with the flight dynamic modes. The model does

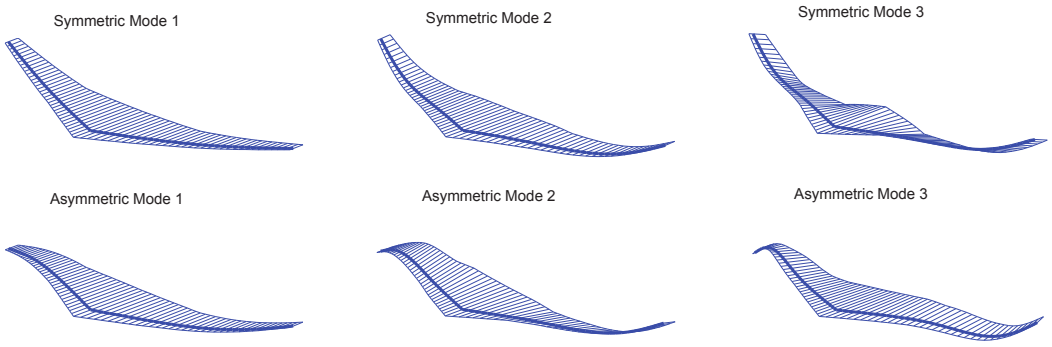

Figure 7: Structural elastic mode shapes of ESAC

however become less accurate at frequencies further away from the preselected frequency, leading to large errors in damping for high frequency aeroelastic modes.

The approximation models show convergence of the pole locations for $n \geq 3$. This can also be seen in Figure 8, where the pole locations for $n \geq 3$ coincide. Although the approximation error decreases with increasing approximation order, no exact convergence of the pole locations can be observed in Tables 4, 5, and 6. The reason for this is that the number of state variables increases due to the addition of aerodynamic lag states, which causes the dynamics matrix to become very large, e.g. the full order ESAC state grows from 415 variables for the frequency-dependent model to 2425 variables for the fifth-order approximation. The calculation of eigenvalues for large asymmetric matrices is numerically sensitive. Consequently, even for very high order approximations no exact convergence can be seen in calculated eigenvalues.

The pole locations corresponding to the first-order model are often relatively far from those corresponding to the higher-order models. In some cases even more so than those corresponding to the frequency-dependent model. For most of the modes, the second-order model is in relatively good agreement with the higher-order models.

B. Flutter Analysis

The model is trimmed at increasing Mach in order to determine the flutter speed for each unsteady aerodynamics approximation. Circulatory aerodynamic coefficients are calculated from a linear potential flow solution that is corrected for compressibility effects at each Mach number. Non-circulatory forces are calculated using linear incompressible piston theory. A solution that takes into account compressibility and transonic effects on all aerodynamic forces could be obtained from an Euler solution for unsteady aerodynamics coupled to a viscous boundary layer model, but would be much more computationally involved to obtain.

The flutter speeds are given in Table 7. Frequency and aerodynamic damping for the first six aeroelastic modes at increasing Mach number are shown in Figures 9 and 10.

In all cases it is the second symmetric mode that goes unstable first. In the frequency-dependent and first-order approximation models the damping of the mode is underestimated, leading to a lower flutter speed. The damping is somewhat overestimated in the second-order model, leading to a slightly higher flutter speed.

Overall it can be seen that for most modes, relatively large discrepancies exist between the frequency-dependent model, the first-order model, and the models using approximations of order $n \geq 2$. In most cases the second-order and third-order approximation models are both very close to the fourth-order and fifth-order approximation models. The latter two models give identical results in almost all cases.

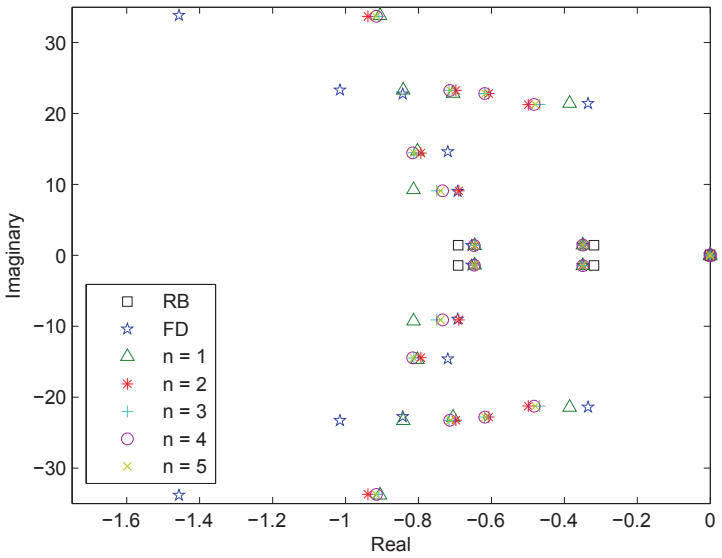

Figure 8: Pole locations of rigid-body (RB) and coupled ESAC for frequency-dependent (FD) at $\omega = 9$ rad/s, and approximation models at Mach 0.797 and 36,000 ft altitude

Table 7: ESAC flutter speed at 36,000 ft altitude for frequency-dependent (FD) at $\omega = 9$ rad/s, and approximation models

n	Flutter speed [Mach]
FD	0.857
1	0.858
2	0.884
3	0.878
4	0.880
5	0.880

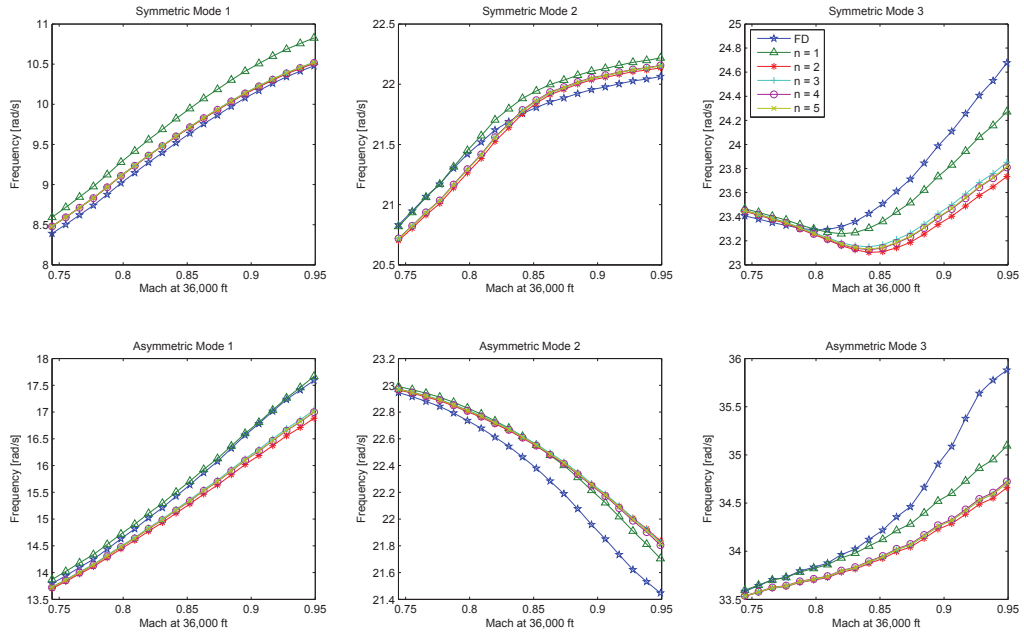

Figure 9: Frequency of ESAC aeroelastic modes for frequency-dependent (FD) at $\omega = 9$ rad/s, and approximation models

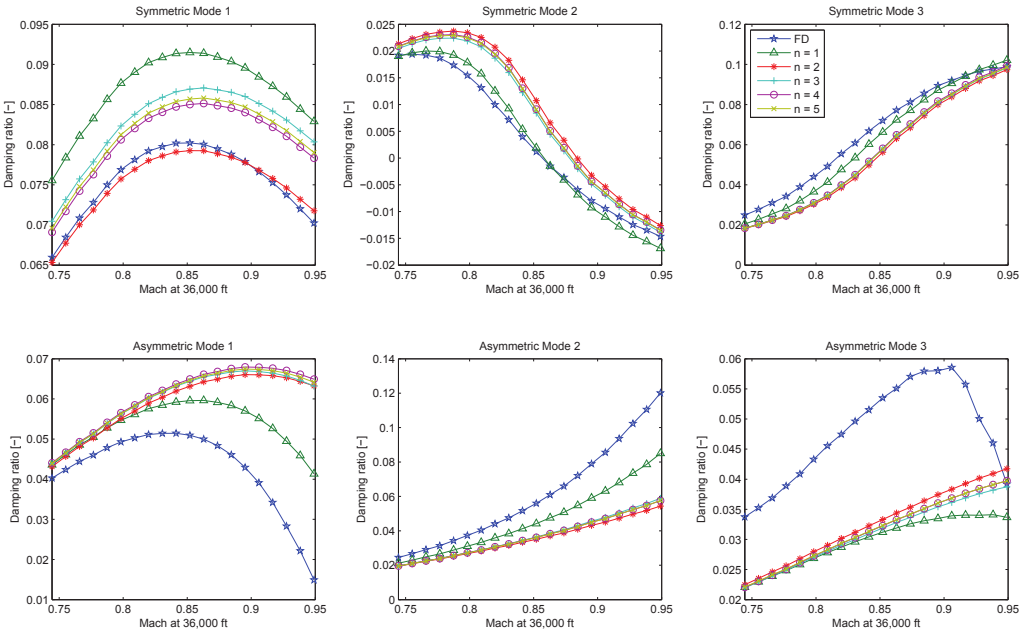

Figure 10: Aerodynamic damping of ESAC aeroelastic modes for frequency-dependent (FD) at $\omega = 9$ rad/s, and approximation models

VII. Numerical Simulation

Numerical simulations were performed using a nonlinear 6DOF flight dynamic model coupled with the full order linear aeroelastic model.

A. Numerical Integration

As simulation is performed using the full order aeroelastic model, aeroelastic modes at very high frequencies (up to the order of 10^4 rad/s) are present. If an inappropriate integration method is used or the time step is not taken sufficiently small this may cause numerical instability.

The location of the poles corresponding to the aerodynamic lag states is dependent on the coefficients of the approximation, the local chord length, and the free stream airspeed. For the nth-order approximation these pole locations are given by

$$\sigma_{i,j} = \frac{2V_\infty p_j}{c_i} \tag{81}$$

where i indicates the wing section and $j \in \{n, n-1, .., 1\}$. The most negative pole location is found for the smallest chord length and thus corresponds to the lag states at the wing tip. An overview of the most negative lag state poles for various approximations is given in Table 8.

Table 8: Most negative pole locations corresponding to ESAC aerodynamic lag states

n	Pole location
1	-44.74
2	-81.44
3	-119.4
4	-159.6
5	-202.7

The stiffness that is introduced into the system of differential equations by the aerodynamic lag states can lead to numerical instability in some, most notably explicit, integration methods. On the other hand, some integration methods, such as the implicit Euler method, introduce numerical damping, which can lead to numerical stabilization of unstable modes. In order to address both of these potential issues, Newmark-β[23] was selected the as integration method.

By selecting coefficients $\beta = 0.25$ and $\gamma = 0.5$, constant acceleration is assumed. Using these coefficients the method is unconditionally stable, has a stability region that coincides with the left half plane, and is $\mathcal{O}\left(\Delta t^2\right)$ accurate. In cases where unconditional stability is not required, e.g. for simulation of a reduced order model with only poles at limited frequency, higher accuracy can be obtained by selecting different coefficients.

The coupled system consists of linear second-order differential equations for the elastic wing, linear first-order differential equations for the aerodynamic lag states, and nonlinear first-order differential equations for the aircraft dynamics and kinematics. The linear system is integrated using a hybrid scheme that combines the Newmark-β method for second-order equations with a second-order multistep method for the linear first-order equations. In case $\beta = 0.25$ and $\gamma = 0.5$ are selected, this scheme is equivalent to the trapezoidal rule with constant acceleration for the second-order equations and constant speed for the first-order equations. The nonlinear differential equations are integrated using a fourth-order Runge-Kutta scheme.

B. Computational Cost

The total number of aerodynamic lag states N for the flexible wing model is given by

$$N = 2 \times n \times (m+1) \times d \tag{82}$$

where n is the order of the unsteady aerodynamics approximation, $(m+1)$ is the number of FEM nodes on the wing, and d is the number of degrees of freedom per node. Similar to the wing deflection state

the aerodynamic lag states can also be transformed into modal coordinates. In that case the number of aerodynamic lag states is given by

$$N = 2 \times n \times m \tag{83}$$

where m is the number of aeroelastic modes.

In both cases the number of aerodynamic lag states is proportional to the order of the approximation. For higher order approximations this can lead to a large increase in the size of the dynamics matrices, e.g. if the lag states are expressed in modal coordinates a fourth-order approximation will add 144 aerodynamic lag states to a system that includes 18 aeroelastic modes.

Additionally, aerodynamic lag states are required to model the unsteady aerodynamics of high-bandwidth control surfaces. For the VCCTEF, which has 32 high-bandwidth flap segments, a fourth-order approximation would add 256 aerodynamic lag states.

The addition of a large amount of aerodynamic lag states to the system will increase computational cost of simulations and other computations. The order of approximation should therefore be selected keeping in mind the required accuracy and the maximum acceptable system size. One could for example use a reduced order model with a low order approximation for controller design, while using a full order model with a higher order approximation to evaluate controller performance.

C. Dynamic Responses

Simulations were performed in order to assess the influence of the unsteady aerodynamics approximations on the dynamic responses of the ESAC. The simulations are initialized in cruise condition at Mach 0.797 and 36,000 ft altitude. Due to its joining to the elastic wing, the VCCTEF is well capable of exciting various aeroelastic modes. The flight dynamic response to a 2×5 s asymmetric VCCTEF doublet followed by a 2×15 s symmetric VCCTEF doublet is shown in Figure 11. The corresponding responses of the first three symmetric and the first three asymmetric elastic wing modes are shown in Figures 12 and 13, respectively.

The VCCTEF doublet consists of a semi-sinusoidally shaped deflection on each wing. The deflection shape is shown in Figure 14. The deflection is equal for both wings in the case of a symmetric doublet, and opposite in the case of an asymmetric doublet.

Figures 11, 12, and 13 show dynamic responses for the frequency-dependent and fifth-order approximation models. While the difference in responses between the frequency-dependent and frequency-independent models is clearly visible, the difference amongst the frequency-independent models is more subtle and cannot easily be seen in time-domain response plots. Close examination lead to the conclusion that the response of the first-order approximation does significantly deviate from higher-order approximations, the second-order approximation is very close to higher-order approximations, and the approximations of order $n \geq 3$ are practically the same. In order to preserve clarity in the figures it was chosen to only show the fifth-order approximation here.

The coupling of aeroelastic and flight dynamic modes is clearly observable in the pitch rate and roll rate responses in Figure 11. Figures 12 and 13 show the excitation of respectively symmetric and asymmetric modes at the moments corresponding to their respective doublet inputs. Examination of these figures confirms that over- and underestimation of the modal damping in the frequency-dependent model as shown in Figure 10 do indeed lead to respectively faster and slower settling of the corresponding mode as compared to the fifth-order approximation model.

In order to better visualize the differences between various approximations, the frequency responses in pitch rate and roll rate to respectively symmetric and asymmetric VCCTEF inputs were computed. These responses are shown in Figures 15 and 16.

The flight dynamic and aeroelastic modes can easily be observed in the response plots. The modes that are listed in Tables 4, 5, and 6 are indicated in the plots.

The frequency-dependent model is again distant from the frequency-independent models. The frequency-independent models are close, but some variation can be observed. In order to further examine this variation the differences of the various frequency-independent models with regard to the 5th-order model are shown on a linear scale in Figures 17 and 18. The difference is given by

$$\Delta_n(\omega) = \frac{|F_n(\omega) - F_5(\omega)|}{|F_5(\omega)|} \tag{84}$$

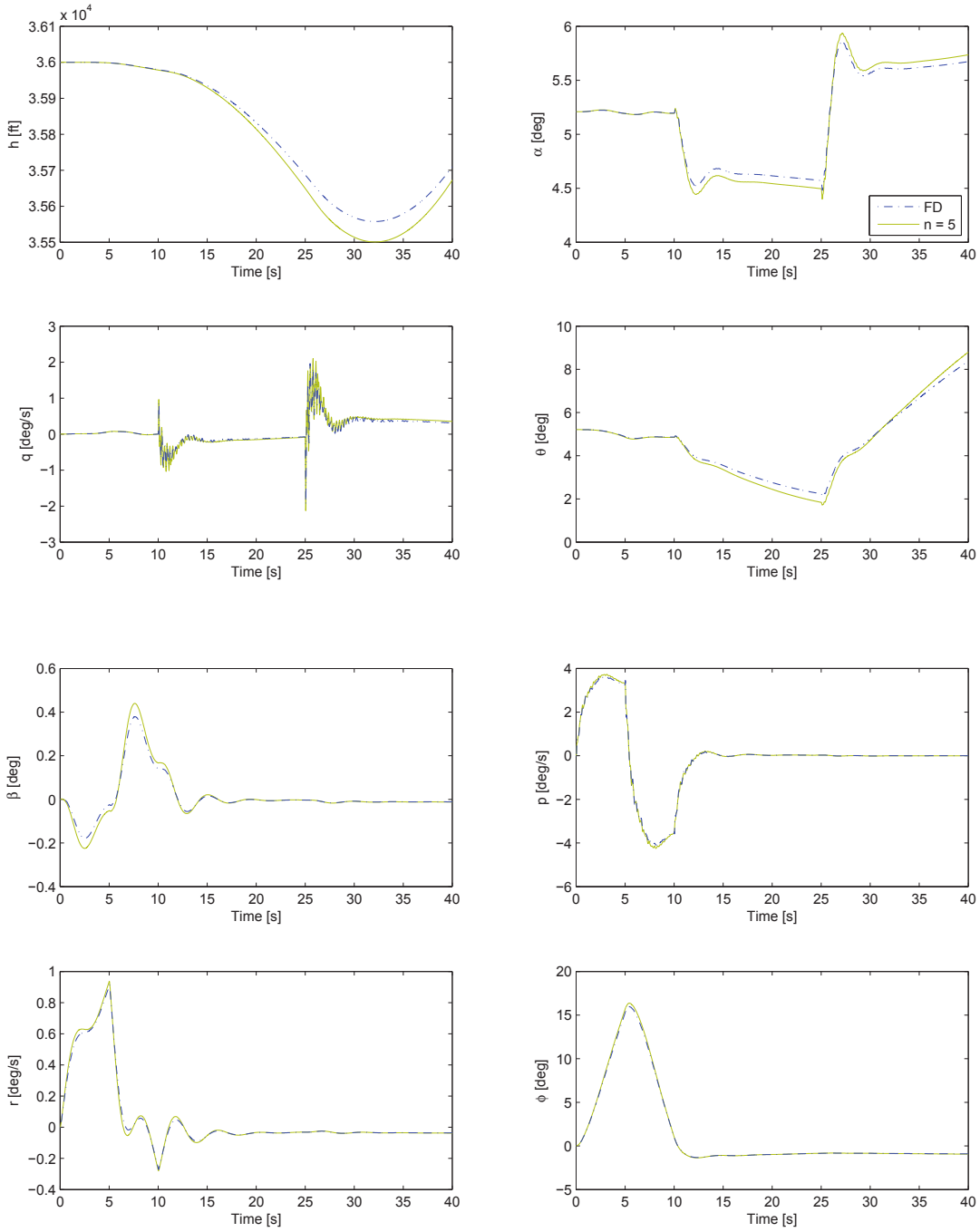

Figure 11: Flight dynamic response of ESAC to a 2×5 s asymmetric VCCTEF doublet followed by a 2×15 s symmetric VCCTEF doublet for frequency-dependent (FD) at $\omega = 9$ rad/s, and fifth-order approximation models

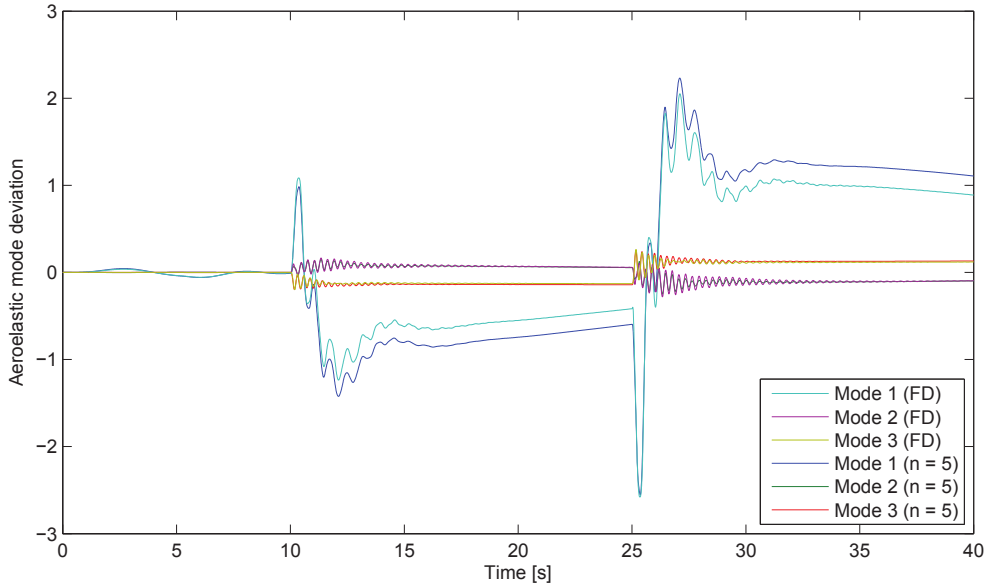

Figure 12: Dynamic response first three symmetric aeroelastic modes of ESAC to a 2×5 s asymmetric VCCTEF doublet followed by a 2×15 s symmetric VCCTEF doublet for frequency-dependent (FD) at $\omega = 9$ rad/s, and fifth-order approximation models

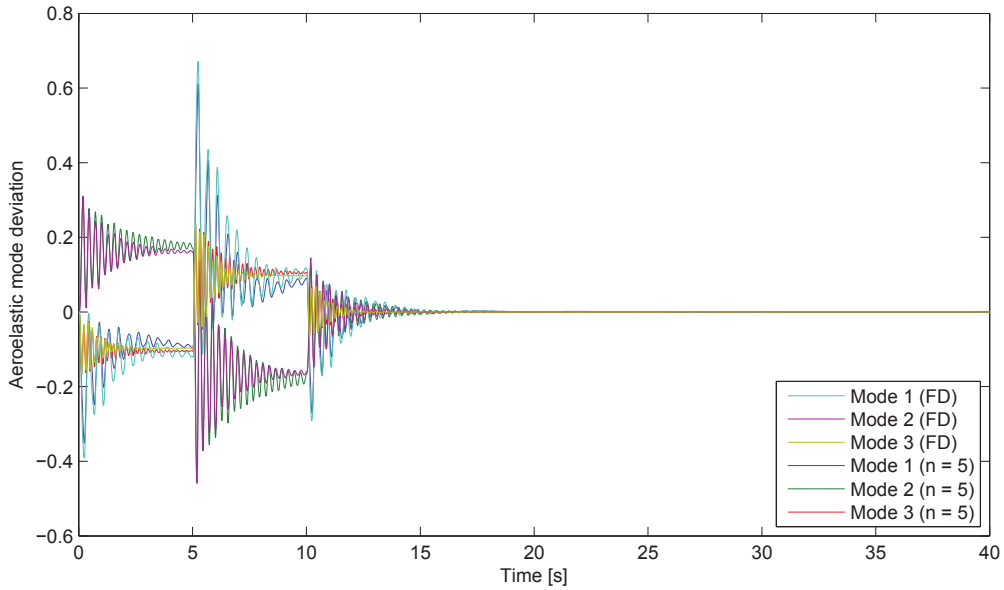

Figure 13: Dynamic response first three asymmetric aeroelastic modes of ESAC to a 2×5 s asymmetric VCCTEF doublet followed by a 2×15 s symmetric VCCTEF doublet for frequency-dependent (FD) at $\omega = 9$ rad/s, and fifth-order approximation models

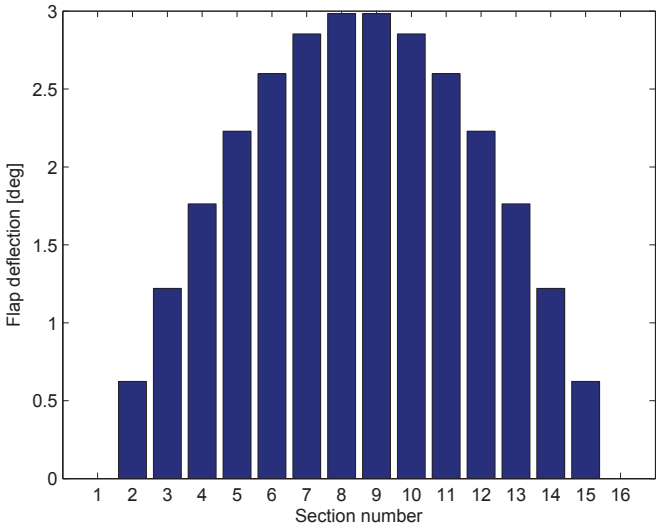

Figure 14: VCCTEF semi-sinusoidally shaped deflection

where $F_n(\omega)$ is the complex-valued frequency response function corresponding to the nth-order approximation model.

It can now clearly be seen that the difference is indeed the largest for the first-order approximation. The second-order approximation is much closer to the higher-order approximations. The differences for the third and fourth-order approximations are again smaller, but the decrease is much less.

VIII. Conclusion

This paper presents a method to obtain a rational fraction approximation of Theodorsen's function based on mixed real and complex linear regression. Results of the regression method are shown and applied to derive a frequency-independent state-space equation for the ESAC wing dynamic aeroelasticity by means of aerodynamic lag states.

A comparison of several frequency-independent state-space models using different order approximations of Theodorsen's function, along with a frequency-dependent model, was performed. The frequency-dependent model contains a misrepresentation of the unsteady aerodynamics at frequencies other than the preselected frequency. This was found to result in a significantly different dynamic response of the coupled flight dynamic and aeroelastic model, justifying the usage of additional aerodynamic lag states in order to formulate a frequency-independent aeroelastic model.

As the order of the approximation of Theodorsen's function increases, the accuracy of the solution increases. However, the number of aerodynamic lag states increases as well, leading to an increased amount of states. Hence, selection of the appropriate order of approximation is a trade-off between computational cost and numerical issues corresponding to simulation, analysis, control design etc. of a dynamical system with an increased number of states on one hand, and the accuracy of the unsteady aerodynamics approximation on the other hand.

In both the frequency domain and the time-domain it was found that the second-order approximation results in a significant increase in accuracy compared to the first-order approximation. The third-order approximation provides another slight increase in accuracy. Approximations of order greater than three provide minimal increase in accuracy compared to the third-order model.

It can be concluded that in case of the described ESAC model, the second-order approximation provides a reasonable compromise between the achieved accuracy and the required number of aerodynamic lag states.

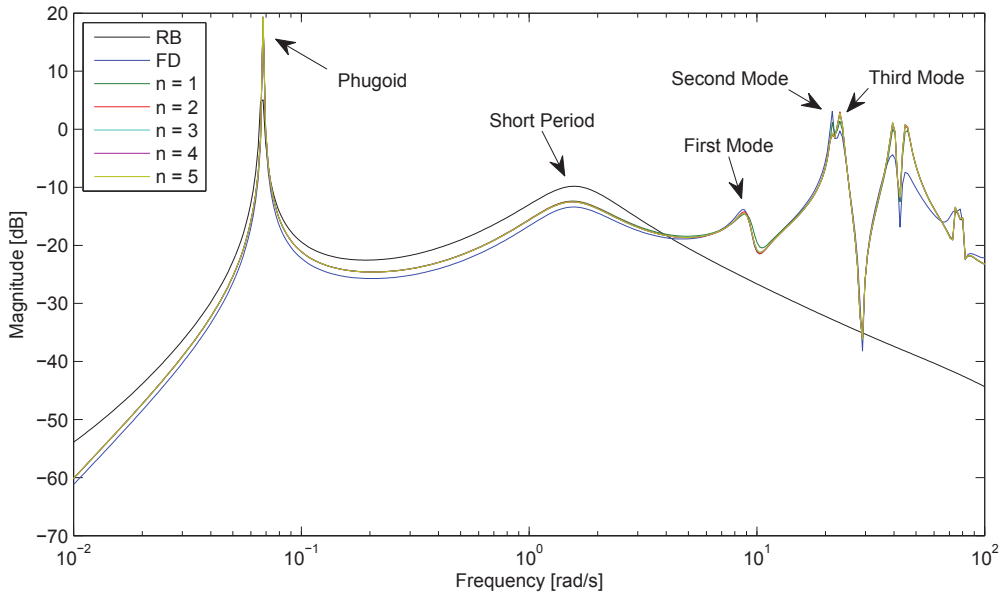

Figure 15: Pitch rate frequency response of ESAC to a symmetric semi-sinusoidally shaped VCCTEF input for rigid-body (RB), frequency-dependent (FD) at $\omega = 9$ rad/s, and approximation models

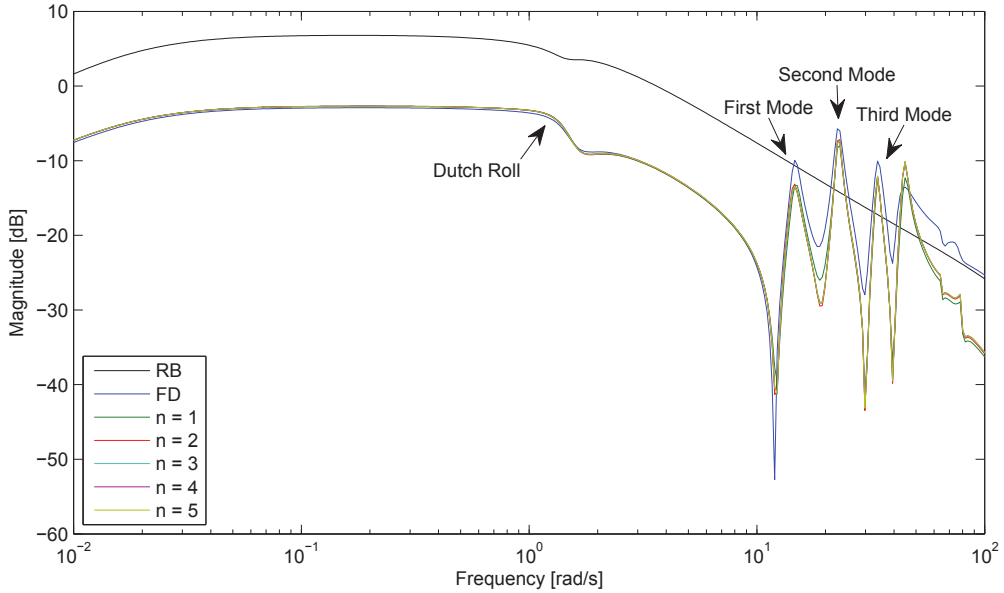

Figure 16: Roll rate frequency response of ESAC to an asymmetric semi-sinusoidally shaped VCCTEF input for rigid-body (RB), frequency-dependent (FD) at $\omega = 9$ rad/s, and approximation models

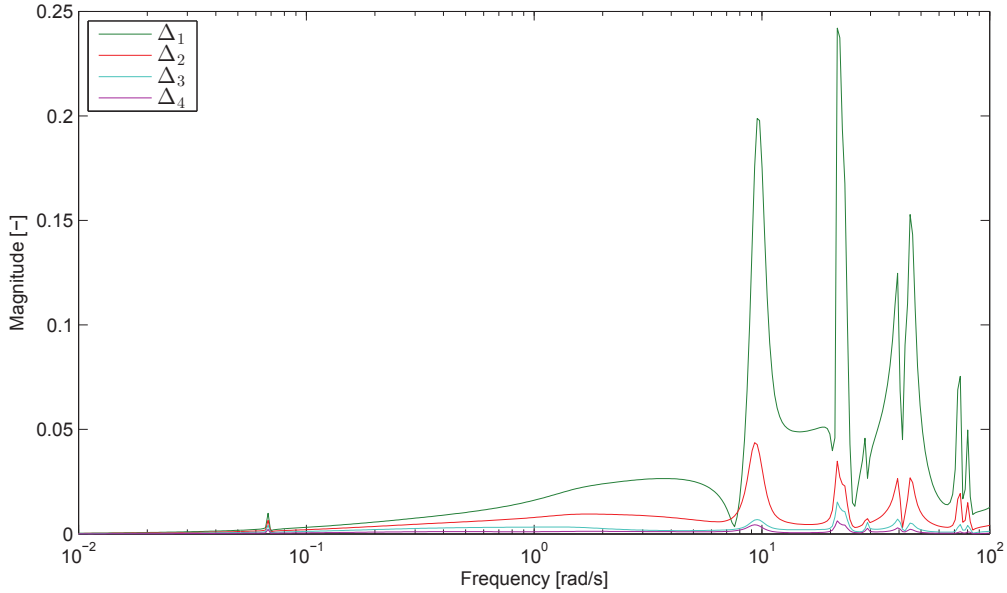

Figure 17: Relative difference in pitch rate frequency response of ESAC to a symmetric semi-sinusoidally shaped VCCTEF input for approximation models

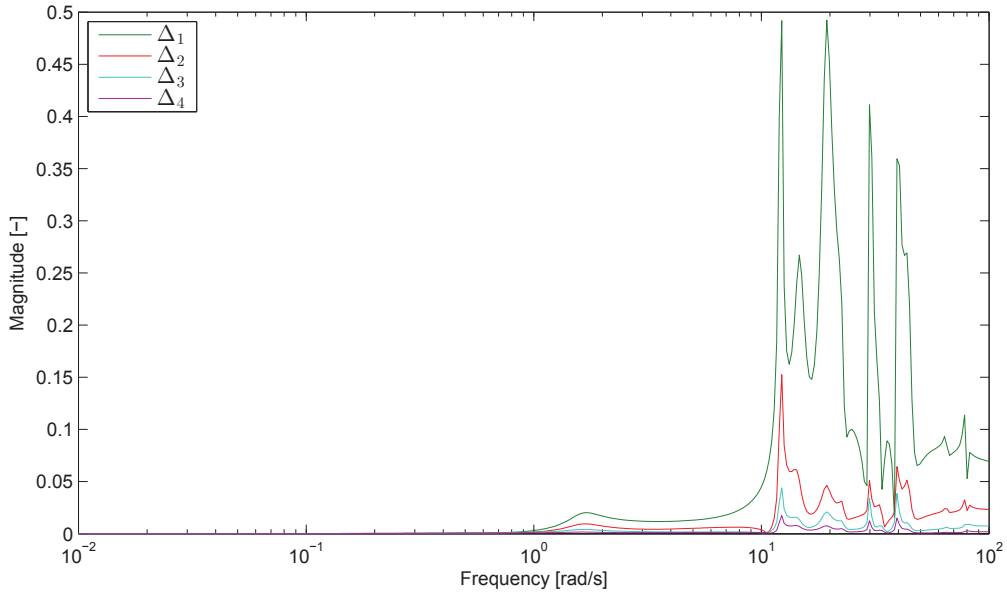

Figure 18: Relative difference in roll rate frequency response of ESAC to an asymmetric semi-sinusoidally shaped VCCTEF input for approximation models

IX. Acknowledgment

The authors wish to acknowledge the NASA Aeronautics Research Mission Directorate (ARMD) Fixed Wing/Advanced Air Transport Technology Project under the Fundamental Aeronautics Program for providing funding support of this work.

References

[1]Nguyen, N., "Elastically Shaped Future Air Vehicle Concept," Tech. rep., NASA Innovative Partnerships Program, 2010.

[2]Nguyen, N., Trinh, K., Reynolds, K., Kless, J., Aftosmis, M., Urnes, J., and Ippolito, C., "Elastically Shaped Wing Optimization and Aircraft Concept for Improved Cruise Efficiency," *51st AIAA Aerospace Sciences Meeting*, 2013.

[3]Noll, T., Brown, J., Perez-Davis, M., Ishmael, S., Tiffany, G., and Gaier, M., "Investigation of the Helios Prototype Aircraft Mishap," Tech. rep., NASA, 2004.

[4]Baker, M. L., Goggin, P. J., and Winther, B. A., "Aeroservoelastic Modeling, Analysis, and Design Techniques for Transport Aircraft," *RTO AVT Specialists' Meeting on Structural Aspects of Flexible Aircraft Control*, 1999.

[5]Lee-Rausch, E. M. and Batina, J. T., "Wing Flutter Computations Using an Aerodynamic Model Based on the Navier-Stokes Equations," *Journal of Aircraft*, Vol. 33, No. 6, 1996, pp. 1139–1147.

[6]Silva, W. A. and Raveh, D. E., "Development of Unsteady Aerodynamic State-Space Models from CFD-Based Pulse Responses," *42nd AIAA/ASME/ASCE/AHS/ASC Structures, Structural Dynamics, and Materials Conference and Exhibit*, 2001.

[7]Edwards, J. W., *Unsteady Aerodynamic Modeling and Active Aeroelastic Control*, Ph.D. thesis, Stanford University, 1977.

[8]Dunn, H. J., "An Analytical Technique for Approximating Unsteady Aerodynamics in the Time Domain," Technical Paper 1738, NASA, 1980.

[9]Vepa, R., "Finite State Modeling of Aeroelastic Systems," Contractor Report CR-2779, NASA, 1977.

[10]Roger, K. L., *Airplane Math Modeling Methods for Active Control Design*, Structural Aspects of Active Control, AGARD CP-228, 1977.

[11]Theodorsen, T., "General Theory of Aerodynamic Instability and the Mechanism of Flutter," Tech. Rep. 496, NACA, 1935.

[12]Nguyen, N., Ting, E., and Trinh, K., "Flight Dynamic Modeling and Stability Analysis of Flexible Wing Generic Transport Aircraft," *55th AIAA/ASME/ASCE/AHS/SC Structures, Structural Dynamics, and Materials Conference and Exhibit*, 2014.

[13]Wagner, H., "Über die Entstehung des dynamischen Auftriebes von Tragflügeln," *Zeitschrift für Angewandte Mathematik und Mechanik*, Vol. 5, No. 1, 1925, pp. 17–35.

[14]Garrick, I. E., "On Some Reciprocal Relations in the Theory of Nonstationary Flows," Tech. Rep. 629, NACA, 1938.

[15]Jones, R. T., "Operational Treatment of the Nonuniform-Lift Theory in Airplane Dynamics," Tech. Rep. 667, NACA, 1938.

[16]Leishman, J. G. and Nguyen, K. Q., "State-Space Representation of Unsteady Airfoil Behavior," *AIAA Journal*, Vol. 28, No. 5, 1989, pp. 836–844.

[17]Nguyen, N., Nelson, A., and Pulliams, T., "Damage Adaptive Control System Research Report," Tech. rep., NASA, 2006.

[18]"AA241 Aircraft Design: Synthesis and Analysis," http://adg.stanford.edu/aa241/structures/weightstatements.html, Stanford University.

[19]Moret, J.-M., "Fitting of Transfer Functions to Frequency Response Measurements," Tech. Rep. 498/94, Centre de Recherches en Physique des Plasmas, Association Euratom, 1994.

[20]Sears, W. R., "Operation Methods in the Theory of Airfoils in Non-Uniform Motion," *Journal of the Franklin Institute*, Vol. 230, No. 1, 1940, pp. 95–111.

[21]Edwards, J. W., Ashley, H., and Breakwell, J. V., "Unsteady Aerodynamic Modeling for Arbitrary Motions," *AIAA Journal*, Vol. 17, No. 4, 1979, pp. 365–374.

[22]Nguyen, N., Reynolds, K., Trinh, K., and Frost, S., "Coupled Aeroelastic Vortex Lattice Modeling of Flexible Aircraft," *29th AIAA Applied Aerodynamics Conference*, 2011.

[23]Newmark, N. M., "A Method of Computation for Structural Dynamics," *American Society of Civil Engineers Journal of the Engineering Mechanics Division*, Vol. 85, No. 3, 1959, pp. 67–94.